Ice-Ocean Turbulent Exchange in the Arctic Summer Measured by an Autonomous Underwater Vehicle

Article *in* Limnology and Oceanography · September 2008

DOI: 10.2307/40058385

2 authors:

D. R. Hayes
University of Cyprus

James Morison
University of Washington Seattle

Limnol. Oceanogr., 53(5, part 2), 2008, 2287–2308

Ice–ocean turbulent exchange in the Arctic summer measured by an autonomous underwater vehicle

Daniel R. Hayes[1] *and James Morison*
Polar Science Center, Applied Physics Lab, University of Washington, 1013 NE 40th Street, Seattle, Washington 98105

Abstract

The first-ever observed horizontal profiles of summertime ice–ocean boundary layer fluxes were obtained using vertical water velocity, temperature, and salinity collected by an Autonomous Underwater Vehicle during the Surface Heat Balance of the Arctic Ocean (SHEBA) experiment of 1998. Scalars and their vertical fluxes, as well as vertical stability, varied in the horizontal direction with correspondence to changes in the overlying surface. In early summer, fresh meltwater was trapped at the upper ice surface and only entered the ocean through leads. A highly stable fresh layer was formed in the SHEBA lead, which eventually grew to depths greater than the mean draft of the local first-year ice. Near the end of July, a storm removed this layer via shear-generated turbulence, supercritical hydraulic flow speeds, and ice divergence. The mixed layer freshened and deepened at this time. Particularly strong fluxes were observed under and downstream of rough, ridged ice, and properties changed rapidly with distance downstream of leads. The location and signs of the fluxes are suggestive of a mechanism of instability in which fresh surface water is forced under salty water downstream of leads and/or ridges. Simulations from a two-dimensional unsteady model suggest that both mechanical forcing from ice topography and a dynamic instability near downstream lead edges may enhance vertical mixing, particularly when ice velocity is large. The horizontal variability in interfacial fluxes observed at SHEBA may explain the difference between the observed melt rates and those calculated using a bulk relationship because this relationship may not adequately parameterize the large lateral heat fluxes at lead edges and basal heat fluxes under ridge keels.

This paper investigates the distribution of thermal energy and fresh meltwater entering the planetary boundary layer of the Arctic Ocean in summer. The spatial distribution of thermal energy in the Arctic Ocean on relatively small scales is important in understanding the large-scale evolution of the sea ice cover, because water heated by the sun melts the ice cover, which tends to expose more open water and in turn allow more heating in a process of ice-albedo feedback. Ice-albedo feedback at a variety of scales needs to be better understood for accurate modeling of the Arctic sea-ice cover evolution under climate change scenarios (Curry et al. 1995; Perovich et al. 2002*a*). Sea ice-albedo feedback generally has been shown to play a part in the polar amplification of climate warming trends (Manabe et al. 1991).

The vertical fluxes of heat, salt, and momentum at the ocean surface vary spatially because of variation in surface type. Even though they only cover a few percent of the surface, openings in sea ice (cracks, leads, and polynyas) are responsible for much of the energy exchange between the ocean and atmosphere during summer (Maykut and Perovich 1987; Ebert and Curry 1993; Maykut and McPhee 1995). In summer, leads and polynyas absorb >90% of the incident solar radiation, while bare ice transmits less than about 5% of incident solar radiation. Fresh water from melted snow and ice enters the ocean through openings in the sea ice or by percolation through the ice depending on ice permeability (Eicken et al. 2002). Once at the ocean surface, mechanical forcing provided by the surface momentum flux typically mixes the meltwater into the seawater. The momentum flux varies from high values under rough, ridged ice to low values under smoother first-year ice or open water. In some cases of low ice velocity the meltwater does not mix at all as a result of sub-bottom ice layers (false bottoms) or strong stratification (Untersteiner and Badgley 1958; Paulson and Pegau 2001; Eicken et al. 2002). In these cases, the freshwater flux into the ocean can be delayed. Freshwater also enters the ocean through basal melt, which is often stronger under rough ice topography.

The spatial variability of surface fluxes over an ice-covered sea is at odds with assumed boundary conditions of most models of the upper ocean, and the effect of this on simulations is largely unknown. Experimental results show that solar radiation through leads warms the polar-ocean mixed layer in summer (Maykut and Perovich 1987; Ebert and Curry 1993; Maykut and McPhee 1995). However, the ultimate fate of this thermal energy is poorly understood. The energy mainly goes into melting of sea ice (Maykut and Perovich 1987; Maykut and McPhee 1995; Holland et al. 1997), but the proportion between basal and lateral melting of various thickness classes is unclear. Though they concluded that the majority of oceanic heat flux to the

[1] Present address: Oceanography Center, University of Cyprus, P.O. Box 20537, 1678 Nicosia, Cyprus

Acknowledgments

The following agencies supported this work: Office of Naval Research (Grants N00014-96-1-5033 and N00014-98-1-0037) and the field support of the National Science Foundation Office of Polar Programs SHEBA project (OPP-9701831). Russ Light of the Applied Physics Laboratory of the University of Washington provided exceptional engineering and field support. We thank Miles McPhee who contributed data and instruments as well as helpful advice in many aspects of this study. David Smith provided the original three-dimensional model code used in this study, plus support and encouragement in making the changes described. Thanks also to two anonymous reviewers who provided extensive and helpful comments.

ice in the central Arctic comes from solar heating of the mixed layer, Maykut and McPhee (1995) were unable to account for lateral melting, effects of melt ponds, and lateral advection of water heated elsewhere. They showed that the thermal energy of the mixed layer is not strictly dependent on the local history of lead fraction because the relative motion of ice and ocean gives rise to a horizontally variable distribution of mixed-layer temperature often independent of the local rate of heating. Since the oceanic heat flux to the ice depends both on mixed-layer temperature elevation above freezing and local stress, horizontal gradients in heat flux can be large. Furthermore, horizontal variability in Arctic sea-ice melt rate on scales between 10 cm and 100 m, much smaller scales than current model grid cells, has been observed (Wettlaufer 1991).

To gain a better understanding of the effect of spatial variability on the summer ice–ocean boundary layer and heat balance of the ice and ocean, we carried out a summer lead experiment at a drifting Arctic station in July and August 1998. The station was part of the Surface Heat Balance of the Arctic Ocean (SHEBA) experiment. SHEBA was designed to improve our understanding of physical processes controlling the vertical and horizontal exchanges of energy in the ocean–ice–atmosphere system (Uttal et al. 2002). The experiment was executed from the Canadian Coast Guard ship the *Des Groseilliers* which was fixed to an ice floe in the Beaufort Sea from September 1997 until September 1998. Our experiment is unique in having used an Autonomous Underwater Vehicle (AUV) to measure the horizontal distribution of turbulent heat, salt, and momentum fluxes in and around a summer lead. The use of an AUV to address these issues in the summertime ice–ocean boundary layer is an outgrowth of a similar study of wintertime lead convection described by Morison and McPhee (1998). They successfully used the Autonomous Conductivity Temperature Vehicle (ACTV) in the winter Lead Experiment (March and April 1992; LeadEx Group [1993]) to observe under-ice horizontal profiles of temperature, salinity, and turbulent fluxes under and around freezing leads. An AUV allows lead measurements of temperature and salinity to be related to the surrounding mixed layer. Also, an AUV complements under-ice heat-flux measurements at discrete locations and depths in the mixed layer with turbulence sensors because they provide horizontal coverage for all surface types. In addition, mixed-layer horizontal variability can be tied to surface type, which complements vertical profiles of ocean properties.

This paper addresses Arctic mixed-layer evolution and interaction with the surface during the summer melt season. The effects of meltwater retention in leads and its subsequent release in the mixed layer are investigated with AUV data. The observed vertical fluxes of heat, salt, and momentum are tied to surface morphology, and new evidence for a mechanism for vertical mixing in a strong horizontal gradient is presented. Numerical studies are shown to support the idea of enhanced mixing at lead edges, ridge keels, and in regions of horizontal density gradients. The delayed meltwater release and enhanced vertical fluxes resulting from spatial variability are placed in the larger scale context through their influence on the mixed-layer structure and resulting ice-albedo feedback.

Methods

Autonomous Underwater Vehicle—The Autonomous Microconductivity Temperature Vehicle (AMTV) was built to test a Kalman smoothing technique (Hayes and Morison 2002) for measuring horizontal profiles of turbulent properties under sea ice and to take advantage of the technique to understand boundary-layer spatial variability, particularly near and around summer leads. The AMTV carries out preprogrammed missions with trajectories determined by a combination of dead reckoning and homing on acoustic transponders. It is based on the REMotely operated Underwater measurement System (REMUS) vehicle developed at the Woods Hole Oceanographic Institution. The AMTV carries a precision Paroscientific pressure sensor and a Systron Donner Motion Pack package of accelerometers and sensitive pitch, roll, and yaw rate sensors. It employs fast-response Sea-Bird Electronics (SBE), SBE 7-02 microconductivity, and SBE 7-01 microtemperature probes, as well as an upward-looking Tritech precision acoustic altimeter to measure ice draft. It operates at speeds from 1.0 m s^{-1} to 1.6 m s^{-1} under program control.

The Kalman smoothing scheme uses vehicle motion to calculate vertical water velocity. It represents an improvement on the basic approach developed by Morison and McPhee (1998) for the study of winter lead convection with the earlier ACTV. The smoother will estimate the portions of the vehicle's movement resulting from unforced motion of the body (such as that due to the control system) and those ascribed to sensor noise. The vehicle forcing (vertical water velocity) is calculated to account for what remains. Hayes and Morison (2002) show how the vertical water velocity spectra from the AMTV and ACTV vehicle agree with fixed Turbulent Instrument Clusters (TIC) over a broad range of energy-containing length scales when the AUVs sample in the boundary layer upstream of the TIC.

Covariances of vertical velocity (w') with deviations of temperature (T') and of salinity (S') are calculated to estimate vertical heat and salt fluxes along the vehicle path. A realization of turbulence quantities is formed by detrending a segment of data and calculating the covariance estimates of heat flux and salt flux (positive upwards):

$$HF = \rho C_p \langle w'T' \rangle \tag{1}$$

$$SF = \rho \langle w'S' \rangle / 1000 \approx \langle w'S' \rangle \tag{2}$$

The brackets indicate averaging. One hundred meters is about the minimum interval suitable for a realization because in that distance the vehicle is likely to sample a sufficient No. of turbulent eddies to produce meaningful flow statistics. The interval must also be chosen so that variations in fluxes are not obscured by spatial variability in surface forcing. To determine if the correlation between velocity and temperature or salinity is significant over a particular span of data, we calculate the correlations at random lags and assume they are distributed normally. If the observed correlation falls outside of a specified range, it is considered significant (Fleury and Lueck 1994; Morison and McPhee 1998; Lueck and Wolk 1999).

The AMTV vertical velocity spectra are calculated using a multitaper method (Percival and Walden 1993) from 100-m segments of data and are averaged in equally spaced bins on a logarithmic wave-number axis. For each segment, the log of the smoothed weighted spectrum (log ($kS_{ww}[k]$)) is fit with a 10th-order polynomial as a function of the log of wave-number (log k). Spectra of vertical water velocity are useful because they allow the calculation of two key turbulence parameters: mixing length and friction velocity. The mixing length is the vertical scale over which the energy-containing turbulent eddies transport momentum, heat, and salt. The location of the peak in the spectrum of vertical water velocity (cycles meter^{-1}) is taken from the 10th order polynomial fit and used to calculate the mixing length $\lambda = 0.85/(2\pi k_{\max})$ (McPhee 1994). The friction velocity is a key turbulence parameter representing the overturning speed of the energy-containing eddies:

$$u_* \equiv \sqrt{\tau} = \sqrt[4]{\langle u'w' \rangle^2 + \langle v'w' \rangle^2} \tag{3}$$

where τ is the local kinematic stress. Friction velocity can be multiplied by mixing length to produce reasonable estimates of eddy viscosity in the entire boundary layer (McPhee and Smith 1976). The AMTV cannot directly measure friction velocity since the horizontal components of velocity are not available. However, a new indirect method developed by McPhee (2004) is used to calculate friction velocity using the spectra of vertical water velocity. Briefly, the nondimensional spectrum of vertical water velocity (weighted spectral density divided by the square of friction speed) is shown to have a universal shape and level in the inertial subrange (the range of length scales where turbulent production matches dissipation). The proportionality constant is known empirically, so observed weighted spectra can be appropriately nondimensionalized to achieve the universal spectrum (i.e., friction speed is calculated to do just that). Horizontal homogeneity and negligible buoyancy flux are assumed.

Surface Heat Balance of the Arctic Ocean experiment (SHEBA)—The summer lead study at SHEBA was conducted from 10 July (day 191) to 10 August (day 222) 1998. Before the start of study the ship had drifted over the Chukchi Cap, a marginal plateau extending north from Bering Strait and ~500 m deep. The ship drifted north-west-ward off the Cap in late July. The lead measurements were made at Sarah's Lake, a lead that opened in late May in an area of first-year ice previously used as the airstrip about 1 km from the *Des Groseilliers*. The sampling strategy was based on that used in the winter lead study of Morison and McPhee (1998). A hut was placed near the lead edge from which the AMTV was launched with a small gantry and hand-held fixture through a hole cut in the ice. The AMTV motion was monitored with a 100-m baseline acoustic tracking range. Recovery was typically made by means of a homing transponder attached to a vehicle capture-net suspended in the launch hole. The AMTV traveled back and forth at several depths, typically 5–10 m under the lead and surrounding ice. The horizontal range of the AMTV runs was on the order of 1 km. Outlines of the lead measured at different times using a small boat towing an acoustically tracked beacon are shown in Fig. 1. The lead remained approximately the same size and shape for most of July except when a small pair of leads opened adjacent to the original lead on 22 July (day 203). The lead system closed in the first few days of August, then opened to a much larger size by 05 August (day 217), and even larger size by day 219.

At the lead site, two TICs were deployed, each consisting of a set of three orthogonal, partially ducted current meters, a SBE-03 temperature probe, and an SBE-04 conductivity probe (McPhee 1989, 1992). These instruments allow the calculation of variance and covariance in the velocity components, temperature and salinity. In particular, we are interested in the vertical fluxes of heat, salt, and momentum, which are calculated using Eqs. 1, 2, and 3. The sampling rate for the lead TICs was 6 Hz. An averaging interval of 15 min is used in forming the covariances, analogous to the 100-m AMTV segments. The speed of the ice relative to the ocean at the cluster depths must be greater than about 5 cm s^{-1} to overcome the rotor cluster threshold. Also, in practice the salt-flux calculations from the lead site TICs were suspect as a result of the relatively long flushing time of the SBE-4 conductivity sensors at the rather low water velocities we encountered. A rigid stainless steel mast supported the units at set depths (<10 m) near the downstream lead edge. A cluster was typically located at the same depth as the AMTV operating depth so that flow statistics from the TIC could be compared with upstream AMTV segments. The relative ice–ocean velocity at the cluster depths did not generally exceed the threshold except for day 205, corresponding to a small peak in wind velocity, and day 208 when the wind began to increase. The TICs were damaged by a ridging event on day 208. On days 205 and 208 there were clusters at 3.5-m and 5.5-m depth. The lead TIC mast was resurrected on days 219–220, with a single cluster at about 5.5 m.

In addition to the AMTV and TICs, a SBE-19 conductivity-temperature-depth (CTD) probe attached to a small Remotely Operated Vehicle (ROV) was used to measure temperature and salinity in the upper few meters of the ocean under various surface types around the lead site. The ROV had a video link to the hut and a real-time display of the CTD data. Visual ice properties, ice draft, and surrounding water properties were observed and recorded. The pumped CT intake was near the top of the ROV, so that we were able to obtain many short vertical profiles through undisturbed water by driving the ROV to 10–12-m depth and then allowing it to float slowly upward.

Besides the measurements at the lead, basic oceanographic measurements were made from a hut near the ship, which was in nearly continuous operation. An SBE 911+ CTD collected profiles to 150 m several times per day with the exception of a few drop-outs during instrumental problems in July. Data describing the ice–ocean exchange

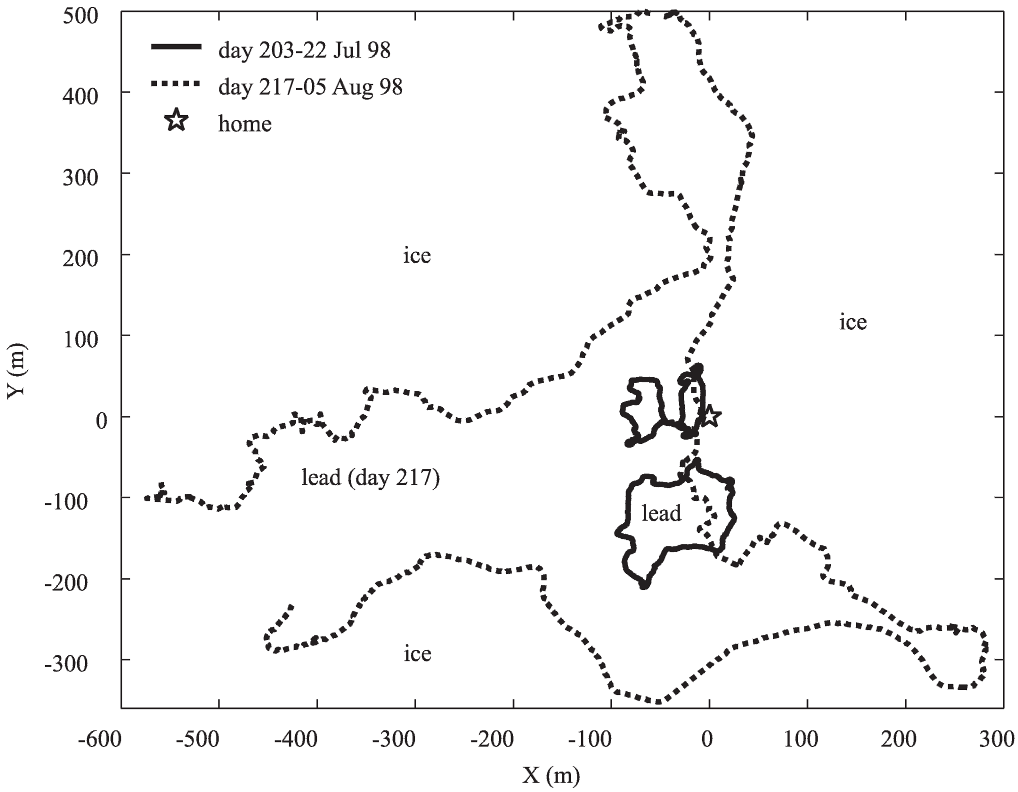

Fig. 1. Outline of the SHEBA lead known as Sarah's Lake on 3 d in 1998. The location of the operations hut is at the origin. Lead perimeter data were collected by tracking an acoustic beacon with the Applied Physics Lab tracking range. The beacon was towed with a small boat. Another lead outline was collected on day 198 (not shown) which was similar to that of day 203 except the two small leads near the origin were not present. The lead on day 217 was not mapped in its entirety.

of momentum, heat, and salt were collected at the same location with TICs. In addition to the partially ducted current meters and SBE-03 and SBE-04 sensors, these TICs included SBE 07-2 microconductivity and SBE 07-1 microtemperature probes and a pressure sensor. The microtemperature and microconductivity probes have a fast response, sampling at 6 Hz and averaging over a 1-s to 4-s period prior to recording to computer disk. The instruments allow the calculation of turbulent fluxes of heat and salt with greater confidence than the standard Sea-Bird probes (McPhee 2004). Low ice speeds and biofouling led to some data drop-outs between days 211 and 215, and for days 219–221 (respectively).

We use a wide variety of the other standard SHEBA measurements. Ice velocities are based on Global Positioning System (GPS) measurements made at the ocean sampling hut. In the calculations and plots here, inertial motion has been removed with a complex demodulation algorithm (McPhee 1986*a*; McPhee et al. 1987; Morison et al. 1987). It has been shown that the interfacial stress caused by inertial oscillations is generally not significant (i.e., the ice and mixed layer tend to oscillate together [McPhee 1986*b*]). Mean velocity is calculated at a time interval of 3 h. Ten-meter wind velocity was measured by the SHEBA Project Office meteorological tower and averaged hourly. The surface coverage by ice, leads, and melt ponds was measured from helicopter photographic surveys throughout the summer (Perovich et al. 2002*b*). The changes in thickness and extent of the ice pack resulting from surface, basal, and lateral melting were observed using thickness gauges at several sites (Perovich et al. 2003).

Results

From an oceanographic point of view, the progression of events during the SHEBA summer can be organized into three phases (shown schematically in Fig. 2): (1) an early period characterized by low wind and ice velocity, a shallow and warming mixed layer, and intense surface melt that collected in leads and ponds, (2) a transition period characterized by high wind and ice velocities and a deepening mixed layer in which fresh surface waters were rapidly mixed away, and (3) and a late period when ice velocity remained high, runoff of meltwater did not accumulate in leads, surface freezing began, and the mixed layer was deeper. These phases will be identified through the calculation of representative bulk estimates as well as observations of the surface conditions. The AMTV data will then be presented against this backdrop of environmental conditions for each phase.

The bulk quantities of Fig. 3 illustrate the progression of air–ice–ocean interaction during the SHEBA summer. Figure 3a shows momentum transfer to the ocean estimated assuming steady-state, free-drift ice motion (McPhee 1990). The ice–ocean friction velocity, u_{*0}, is defined in terms of the ice–ocean surface stress, $\tau_0 = \rho u_{*0}^2$, where ρ is

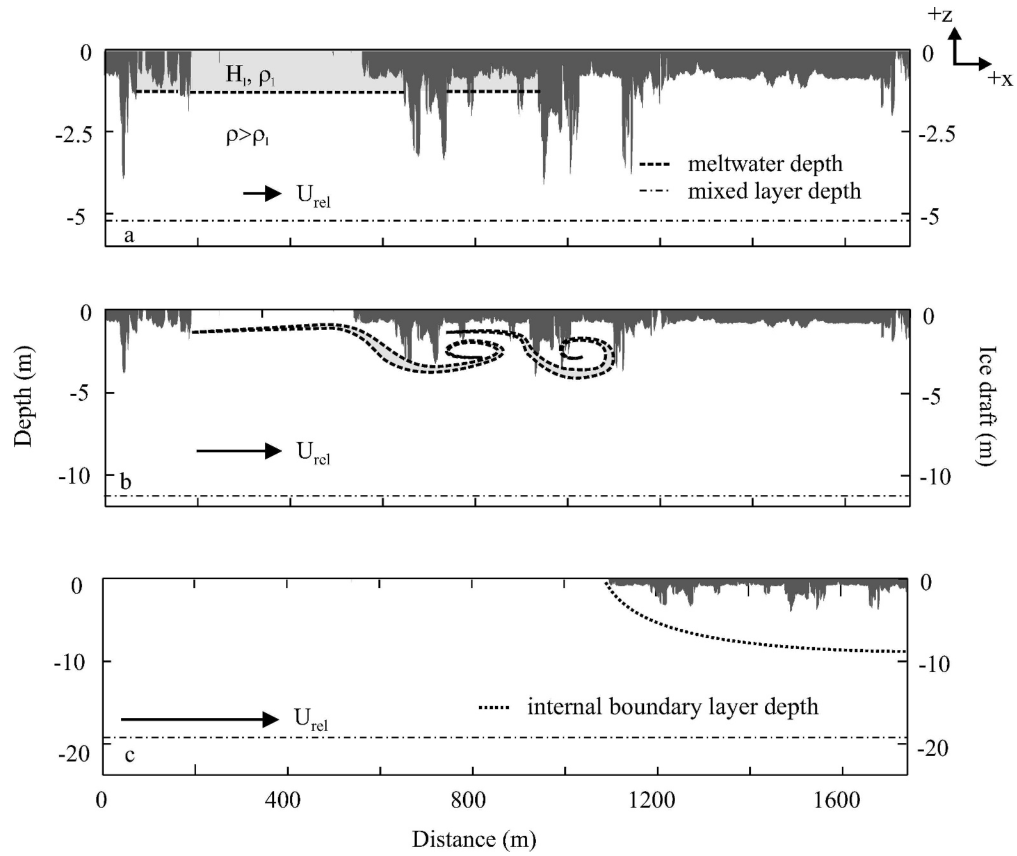

Fig. 2. Schematic of the three phases at SHEBA illustrating the most important upper-ocean characteristics. (a) Ice topography and a lead with low-salinity meltwater layer extending just below mean ice draft (such as for day 206 at the SHEBA lead). The relative ice–ocean velocity was low and mixed layer was shallow. (b) The same ice topography and lead during the time of the meltwater-layer removal (such as for day 213 at the SHEBA lead). Ice velocity is larger, the mixed layer is deeper, and the meltwater layer is hydrodynamically unstable leading to its escape and subsequent mixing with the surrounding seawater. Note the eddies depicted are grossly exaggerated in size and merely indicate the expected sense of the fluxes; in reality, such an eddy should be only about 2 m in diameter (not 200 m as shown). (c) The steady, internal boundary layer (such as for day 220 at the SHEBA lead). Ice velocity is high and the mixed layer is deep. The effect of the new boundary condition propagates downward with downstream distance. Note the different vertical axes.

the water density. The mean surface stress is estimated by applying the 10-m wind speed relative to the ice, U_{10}, and ice speed U_i, to the free-drift ice force balance:

$$\boldsymbol{\tau}_0 = \rho_a C_{Da} \mathbf{U}_{10} U_{10} - if \rho_i h_i \mathbf{U}_i \qquad (4)$$

The density of air, ρ_a, is 1.3 kg m^{-3}; the drag coefficient, C_{Da}, is 1.5×10^{-3}. The drag coefficient was shown to vary from 1.1 to 2.0×10^{-3} during SHEBA (Andreas et al. 2001). This range results in upper and lower bounds on friction velocity during the storm events of $\pm 15\%$ (less during quiet periods). Note that the variability in the drag coefficient outweighs the error introduced by measuring wind speed relative to the ice (moving at about 2% of the wind speed). Density (ρ_i) and thickness (h_i) of ice are ~920 kg m^{-3} and 1 m. The Coriolis parameter, f is about 1.4×10^{-4} s^{-1} at 80°N. Figure 3b indicates the heat available in the mixed layer to melt ice because it is proportional to $\delta T = T - T_f$, the elevation of the temperature, T, above the surface freezing temperature; $T_f = -mS_{4m}$ where S_{4m} is the salinity at 4 m and m = 0.055°C. Temperature and salinity from the main SHEBA CTD site were used. The sensible heat flux (Fig. 3c) can be related to the temperature elevation and the surface stress through an empirical bulk relation, $F_{heat} = \rho C_p \langle w'T' \rangle_0 = c_H \rho C_p u_{*0} \delta T$. The exchange coefficient, c_H is ~0.006 over a wide range of conditions (McPhee 1992); C_p is the heat capacity of seawater at constant pressure (3980 J kg^{-1}). The upward salt flux in the ocean (Fig. 3d) is approximated as that required to balance the downward freshwater flux produced by melting of an isothermal ice floe with a salinity S_{ice} by the ice–ocean heat flux of Fig. 3c, $\langle w'S' \rangle_0 = \langle w'T' \rangle_0 (S_{ml} - S_{ice}) q_l^{-1}$. The ice salinity is taken to be 2 (varies from 0 to 4 depending on ice type and

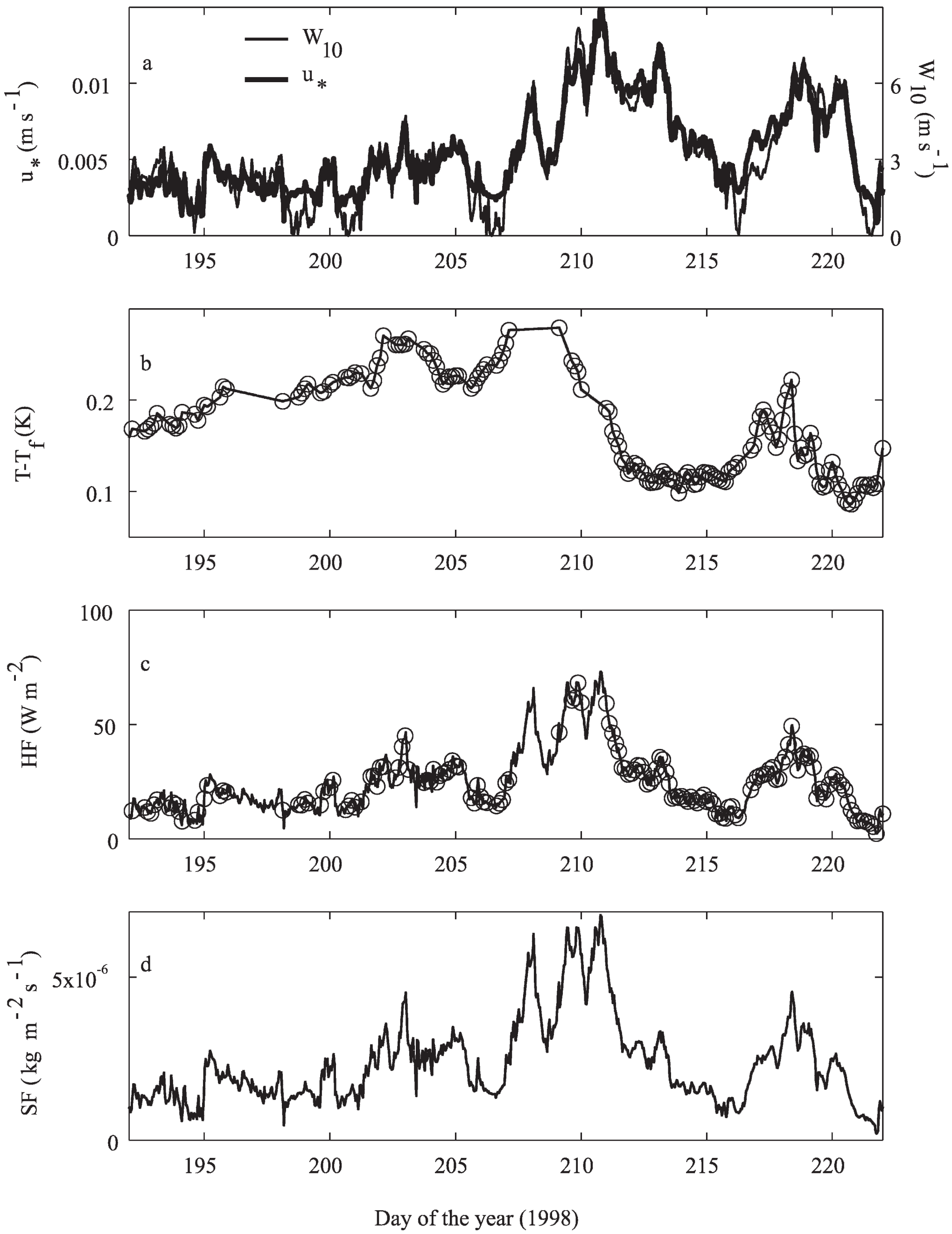

Fig. 3. (a) Friction speed at the ice–ocean interface and wind speed at 10 m from the SHEBA Project Office. (b) Elevation above freezing temperature at 4-m depth. (c) Ice–ocean heat flux from bulk exchange relation, proportional to the product of friction speed and elevation above freezing temperature in panels a and b. The solid line shows heat flux using a mixed-layer temperature that has been interpolated to fill in missing data. The symbols show heat flux when temperature elevation was actually observed. (d) Salt flux at the ice–ocean interface assuming the bulk heat flux goes to melting ice of salinity 2.

vertical position according to Eicken et al. [2002]), and the value of q_l is set at a representative value of 74 K (sea ice latent heat of fusion divided by heat capacity of seawater).

Background oceanographic conditions complete the bulk characterization of the summer period at SHEBA. Figure 4 illustrates bathymetry and upper ocean conditions from the CTD at the main oceanographic site, always far from any leads (>1 km). Bathymetry and salinity contours (Fig. 4a) indicate the sudden mixed layer freshening occurred about the same time as the drift off of Chukchi Cap. The square of the buoyancy frequency, $N^2 = -(g/\rho)(\partial\rho/\partial z)$ where g is the gravitational constant is contoured along with the depth of each run and a special contour representing the mixed-layer depth (Fig. 4b). Potential temperature, θ, contours, and elevation of potential temperature above the surface-pressure freezing point show the gradual mixed-layer warming (Fig. 4c,d).

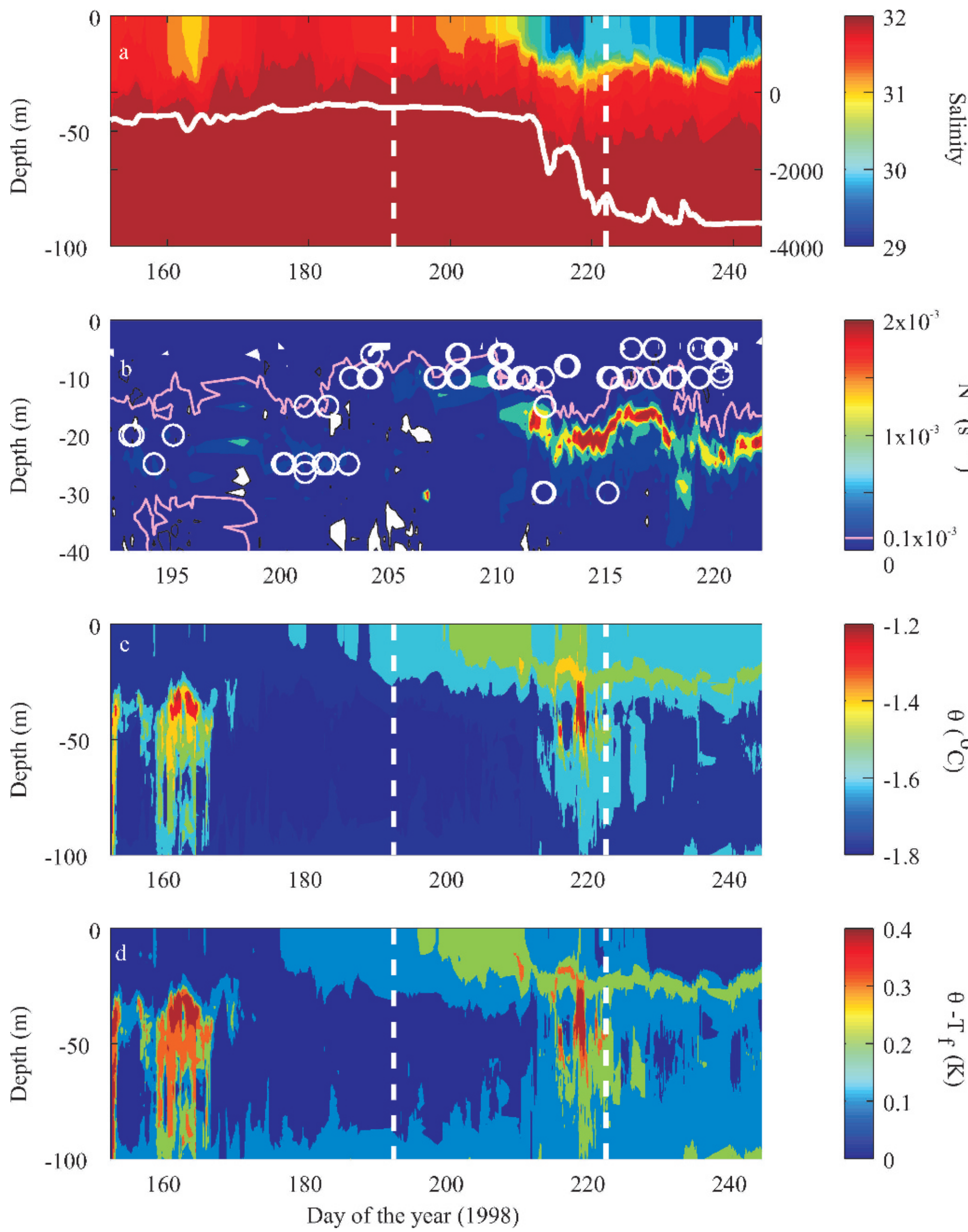

Fig. 4. The bathymetry and contoured water properties during the SHEBA drift for June, July, and August, 1998. (a) Ocean city CTD profiler salinity and ocean depth, (b) square buoyancy frequency in top 40 m along with the 1×10^{-4} s^{-2} contour (pink) and the AMTV run depths and times (circles), only for day 192–221 (c) potential temperature, and (d) potential temperature departure from surface freezing temperature. For (a), the stable salinity gradient below 50 m (contours greater than 32) are not shown in order for ocean depth to be visualized and near-surface changes to be more apparent. Vertical dashed lines indicate the time period shown in panel b.

Environmental data from Period I (day 170 to day 208) show that AMTV runs were all carried out below the gradually warming mixed layer. Wind stress was low. Period II conditions consisted of strong wind stress and a rapidly freshening, deepening mixed layer, all occurring during a drift into deeper water (day 208 to about day 214). After day 214, wind stress was often strong, but the mixed layer was deeper and held near the freezing temperature. The way that the AMTV data relate to these background conditions is now discussed in detail.

Period I: surface traps meltwater—The period of mid-June to late July (day 170 to day 208) was relatively calm: the surface stress and wind were low until a moderate peak centered on day 208, followed by a large, sustained event marking the transitional period of about 210–214 (Fig. 3a). The ice–ocean heat flux was also relatively weak before day 208 (Fig. 3c). Our observations confirm Paulson and Pegau (2001), who found that from day 170 to day 208, snow and ice melt was progressively trapped near the surface in leads and the resulting layer of low-salinity water thinned rapidly

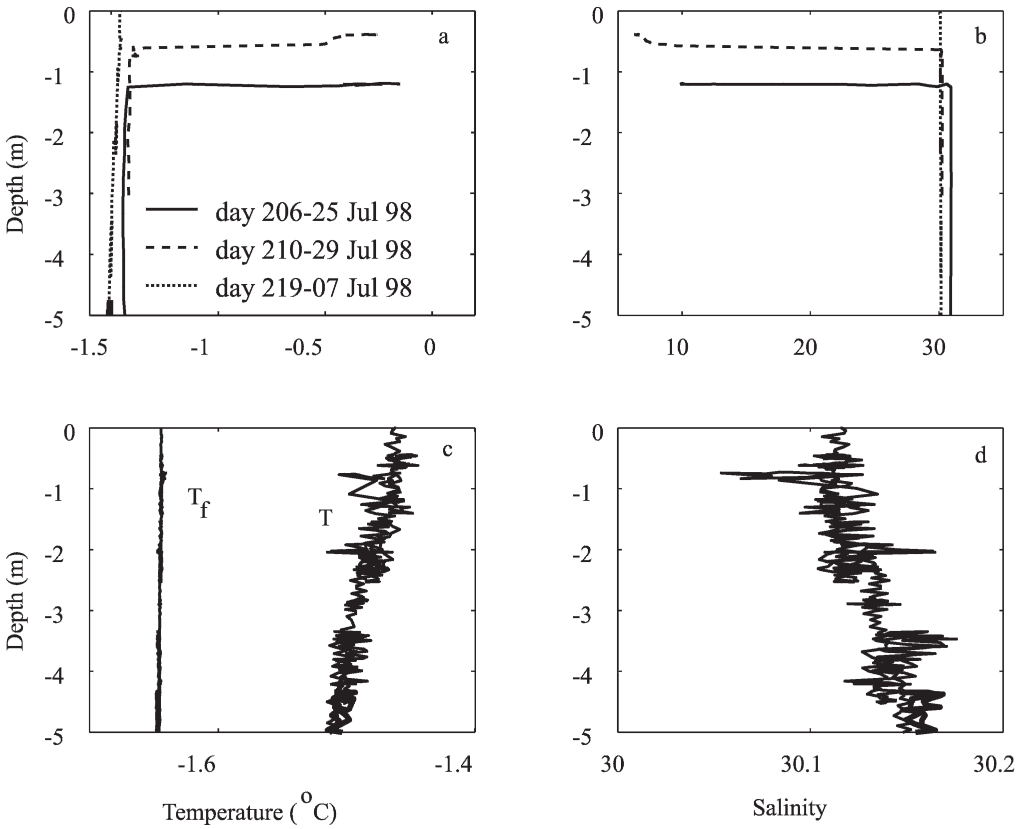

Fig. 5. Remotely-Operated Vehicle profiles of (a) temperature and (b) salinity in the main SHEBA lead. On 25 July 98 (day 206) and 29 July 98 (day 210) the ROV could not float passively to the surface because of the strong stratification in the lead, so the profiles do not extend to the surface. (c, d) The profiles on 07 August 98 (day 219) are shown in detail along with surface freezing temperature.

during the storm on days 210–214. They report the layer ultimately had a salinity of about 2 and a temperature of 1.6°C. We also tracked the depth progression of the freshwater interface in the SHEBA lead with the ROV camera and CTD (Fig. 5a, b). On day 206 (25 Jul) the layer reached a maximum depth of 1.2 m in the lead; the ice draft surrounding the lead was slightly less. The ROV was unable to sample the uppermost part of the layer because it was insufficiently buoyant in the low-density water there, but it could sample under the ice and showed that at its maximum, the fresh water layer extended below the bottom of some of the surrounding ice (show schematically in Fig. 2a). Leads sampled within 30 km of SHEBA on day 203 also had similar warm, fresh layers around 1 m thick (Richter-Menge et al. 2001). At no time was the low-salinity surface layer observed at the main SHEBA CTD site.

From day 152 to day 190 (Jun to early Jul), the mixed-layer temperature and salinity were relatively steady (Fig. 4a,c), yet the surface was rapidly melting (Perovich et al. 2003). In mid-July (days 190–207) the mixed layer warmed in the top 30 m but still did not freshen significantly. The squared buoyancy frequency, N^2, shows the mixed layer shoaled from about 15 m to 6 m in mid-July (Fig. 4b). Other temperature and salinity features during the quiet period were concurrent with the drift over steep bathymetry near the edge of Chukchi Cap over days 161–165 (Fig. 4c,d).

The AMTV data collected prior to day 208 indicate that vertical mixing of temperature as well as momentum was weak (in the range of sampled depths of 5–30 m). Because of microconductivity sensor damage, no salinity-related quantities at the lead are available from the AMTV from day 195 to 212.

Period II: meltwater enters the ocean—Winds associated with the first storm of the summer peaked on day 210 (Fig. 3a), and the mixed layer freshened by >1 (Fig. 4a) between days 209 and 214. The mixed layer cooled to about 0.1 K above the freezing temperature (Figs. 2b, 3d) and deepened from 5 m to 16 m (Fig. 4b). The bulk ice–ocean heat flux was the strongest of the summer from day 208 to day 212 (Fig. 3c). A layer of warm water between 20 m and 30 m in the pycnocline remained through the storm (Fig. 4c). As the camp drifted from Chukchi Cap into deep water during the storm, the pycnocline also freshened at depths of 30–60 m (Fig. 4a).

The observed mixed-layer salinity change of Fig. 4a would require a surface salt flux over day 210–215 an order of magnitude greater than that indicated by the ice-bottom melt rate of Fig. 3d. This is because the rate of change in salt content of the top 30 m includes fresh-water flux resulting from surface melting as well as advective changes unconnected with surface processes. We have estimated the advective rate of change in integrated salt content by assuming the change in salinity at 30 m is unaffected by surface processes, and in the absence of surface processes the salinity profile above 30 m would hold its initial shape. The advective change was subtracted from the actual rate of change of salt content in the top 30 m to obtain the vertical flux resulting from melting at the ice top and bottom surfaces. The total amount of freshening minus the assumed advective change is equivalent to 78 cm of fresh water, or $4.6 \pm 1.5 \times 10^{-5}$ kg m^{-2} s^{-1} from day 210 to day 215. Buoys 20 km from SHEBA showed simultaneous mixed-layer freshening of the same magnitude as the advection-corrected SHEBA CTD (M. G. McPhee pers. comm.) supporting the idea that the SHEBA site drifted through a salinity front at this time.

The transition period is characterized by the removal of the fresh layer of water in the lead. During the first wind event from day 206.5 to day 210.5 (25–29 Jul 98), the layer receded from 120 cm to 65 cm (Fig. 5a,b). This is equivalent to a vertical salt flux of $5.0 \pm 1.0 \times 10^{-5}$ kg m^{-2} s^{-1} over the area of the lead assuming lateral flux was prevented by the ice at the lead edge. During the major wind event from day 210.5 to day 212.5, the remaining 65 cm of fresh water were removed, corresponding to a salt flux of about 12×10^{-5} kg m^{-2} s^{-1} in the lead. Since the lead fraction was about 5%, the spatially averaged fluxes would not be enough to account for the observed salinity changes. The effect of ice convergence or divergence on the thickness of the freshwater layer is unknown, but it should be noted that it has been calculated (Stern and Moritz 2002). Those authors indicate the ice in a 50×50-km box surrounding the SHEBA site diverged 2.5% day^{-1} starting on day 210, and the divergence remained positive for the next several days. In any case, the mixed-layer change cannot be attributed solely to the removal of the fresh layer in leads. Basal melt, surface melt, and release of fresh water stored in melt ponds and the ice interior (Eicken et al. 2002) are required in addition to lead flushing to explain the decrease in mixed layer salinity.

The AMTV results from the flushing period are best characterized by the strong heat fluxes upward under rough ice from day 210 to day 213 and the unusual result on day 213 when these strong heat fluxes occurred with *downward* salt fluxes under a ridge keel. No AMTV salinity data are available before day 213.

On day 213 the first significant wind event was in progress, with wind speeds of >8 m s^{-1}. The ice cover shifted around changing the geometry of the lead. Open-water sections observed by the AMTV altimeter were no wider than 50 m (Fig. 6a). The AMTV was at a depth of 8 m, and observed a mean ice draft of about 1 m with a ridge keel approaching 4-m depth encountered in the last half of segment 2 and the same one on the return journey, halfway through segment 3 (Fig. 6a,c). Large momentum, heat, and salt fluxes were observed under and downstream of this ridge keel (run coordinates 500–1100 m; Fig. 7). The average heat flux was higher than the bulk estimate: 51 W m^{-2} upward for segments from 500 m to 1100 m in Fig. 7a. Salt flux averaged 0.59×10^{-5} kg m^{-2} s^{-1} *downward*, again a surprising observation in the absence of sea-ice formation (Fig. 7b). The downward salt flux occurs despite the average upward salt flux during days 210–215 if one assumes the bulk upward heat flux causes melting. Friction speed (Fig. 7c) was above the surface value of Fig. 3, and particularly high for segments under and downstream of the ridge. The friction speed was 2–3 times larger than AMTV observations during the quiet period (not shown). Maximum mixing length from vertical water velocity spectra was steady at 1.0 m, except for two extrema during the run at 1.5 m and one at 0.2 m. A repeat of this run a few hours later showed even stronger upward heat flux and downward salt flux under regions of ridge keels separated by small, 50–60-m leads. In the two legs between 900 and 1400 m in the second run, upward heat fluxes of 100 W m^{-2} and 135 W m^{-2} and downward salt fluxes of -4.4 and -6.0×10^{-5} kg m^{-2} s^{-1} were observed. Although surprising, these seemingly inconsistently large and reverse fluxes can be explained by small-scale mixing processes involving the low-salinity surface layer. Note that these were the first runs to take place after the fresh layer in the lead had disappeared.

From day 207 to day 213 (25 Jul to 01 Aug 98), vertical heat flux in the boundary layer increased from values of a few W m^{-2} to the large AMTV values presented above. Figure 8 shows panels of ice topography and series of heat flux for all runs at depths of ≤ 10 m during this period. The lead at this time was small and a No. of ridge keels of 2–4-m draft were present. In each panel average fluxes over 100-m segments are calculated over each straight and level leg of the runs on that day. When more than one run exists for a given day, and the run tracks are similar, each leg has been averaged and plotted with a black horizontal bar. No significance testing was carried out before averaging. While the wind increased from day 207 and remained high until day 214, heat fluxes were small until day 210. At this point, the upward heat fluxes began to strengthen. It is curious that the bulk surface heat-flux predictions seem to peak earlier than the AMTV observed mixed-layer values, although the observation that the highly stable fresh water layer persisted at the ocean surface until day 212.5 (even 65 cm thick on day 210.5) will help explain how this can be.

Period III: quasi-steady boundary layer—A brief quiet period around day 214–217 was followed by another wind event from 218 to 220 (Fig. 3a). A rise in mixed-layer temperature during the quiet period followed by a wind increase led to a smaller, briefer pulse of heat flux around day 218, according to bulk calculations (Fig. 3c). The mixed-layer salinity and temperature were otherwise relatively steady (Fig. 4a,c), and the mixed-layer depth was mainly around 20 m (Fig. 4b). The layer of warm water in the upper pycnocline was maintained following the major storm and throughout the rest of the summer: the mixed layer was within 0.1 K of the freezing temperature, while the pycnocline was about 0.2 K above freezing (Fig. 4d). A subsurface temperature maximum, possibly related to topographically steered currents along the shelf slope, was observed over the sloping bathymetry (Fig. 4c) as camp continued to drift off Chukchi Cap.

In the post-storm period, meltwater was not trapped near the surface but mixed downward as the melting occurred. The fresh layer of meltwater did not reappear. The

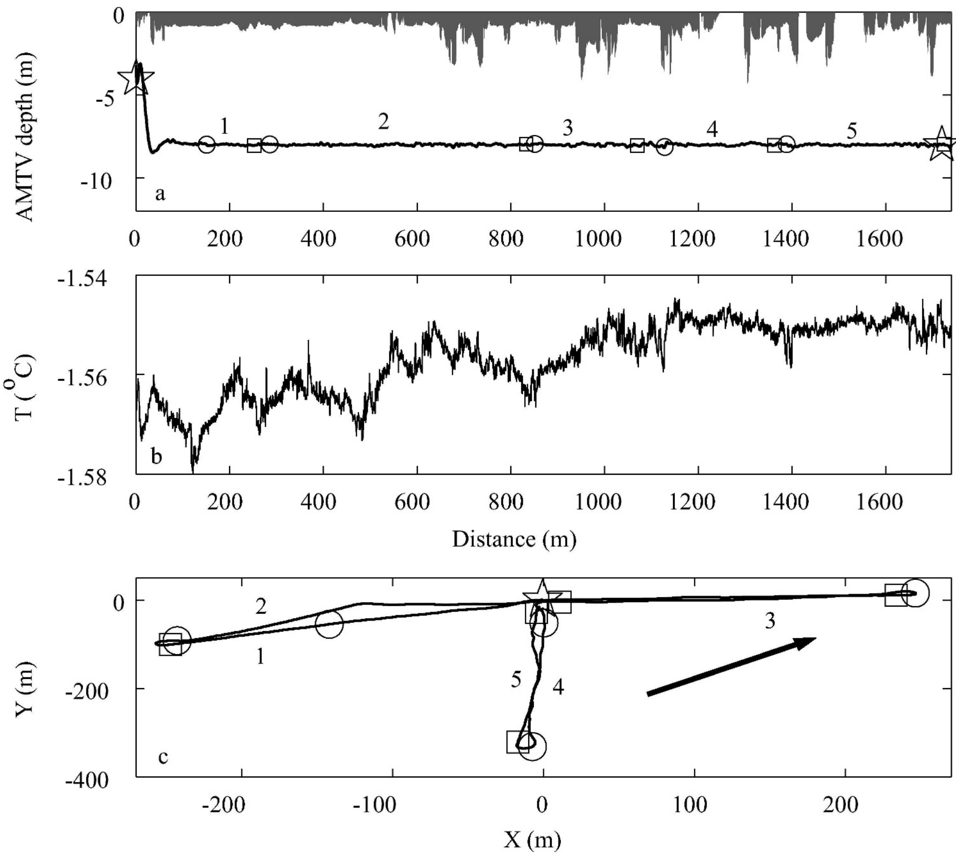

Fig. 6. AMTV run on day 213.0 (UT). (a) Vehicle depth: the circles and squares indicate the beginning and end of each run segment to be analyzed, respectively. On these legs the AMTV was not making large depth or heading changes, allowing one to obtain vertical water velocity using the Kalman smoother. Also shown is the ice draft from the AMTV's upward-looking acoustic altimeter (shaded area at top). (b) Temperature observed by the AMTV. (c) Horizontal position of the AMTV as recorded by an acoustic tracking range. The *x*- and *y*-axes are defined in the tracking range software and were fixed to the local floe throughout the experiment. The star represents the starting point of the run, the same symbols as in panel a are used to indicate the segments of the run to be analyzed. The ice velocity (from demodulated GPS data) is shown: 0.21 m s^{-1}. The length of the arrow corresponds to the distance the ice traveled in 1000 s. The AMTV crossed a ridge at around +200 m on the *x*-axis.

lead profiles of temperature and salinity generally resemble the day 219 (07 Aug) profile in Fig. 5. A detailed view (Fig. 5c,d) shows the lead surface had weak gradients, was stably stratified, and was above the freezing temperature.

After the major wind event of the SHEBA summer, strong fluxes of momentum were observed in the lead and under ice, and strong heat and salt fluxes were observed in the lead. The last day of AMTV observations was day 220. The wind had increased again after a few days of relative calm, and the lead had grown dramatically in size around day 215. On day 219.9, the temperature at the run depth (5 m) increased as the lead edge was approached from upstream, peaked at the edge, and then fell with distance under the ice (Fig. 9b). Nearly the same trends were observed on both the out and back legs. The salinity shows freshening as the lead edge was approached (Fig. 9c), but the rate of change itself is not reliable because of a nonlinear drift in conductivity. Heat fluxes were downward and salt fluxes were upward under the lead (Fig. 10a,b). The cumulative effect of the vertical convergence of fluxes on a particular water parcel traversing the lead was warming and freshening. At downstream distances greater than about 100 m under the ice, fluxes were smaller. Friction speed was close to the surface value, and it increased under the ice (Fig. 10c). Maximum mixing length averaged around 0.7 m with a maximum of 1.8 m at the lead edge.

Bulk, TIC, and AMTV intercomparison—The AMTV can accurately measure ice–ocean stress. While the AMTV-derived friction speeds vary greatly over any given run, the run averages agree with the steady-state force balance estimate (Fig. 11). The average is computed from the 100-m segment values like those of Fig. 10. Agreement with the surface friction speed is good. Agreement with the lead-edge TIC is not as good: the TIC shows friction speeds generally at or above the AMTV and average surface values. The AMTV samples many surface types, so it arguably provides a measurement of stress that is more representative of the spatial average. Point measurements of stress near the downstream lead edge should be representative of stress in the lead but the surface discontinuity of the edge may enhance stress locally.

Except for day 213, when heat flux run averages were upward, they were less than the surface value (Fig. 12),

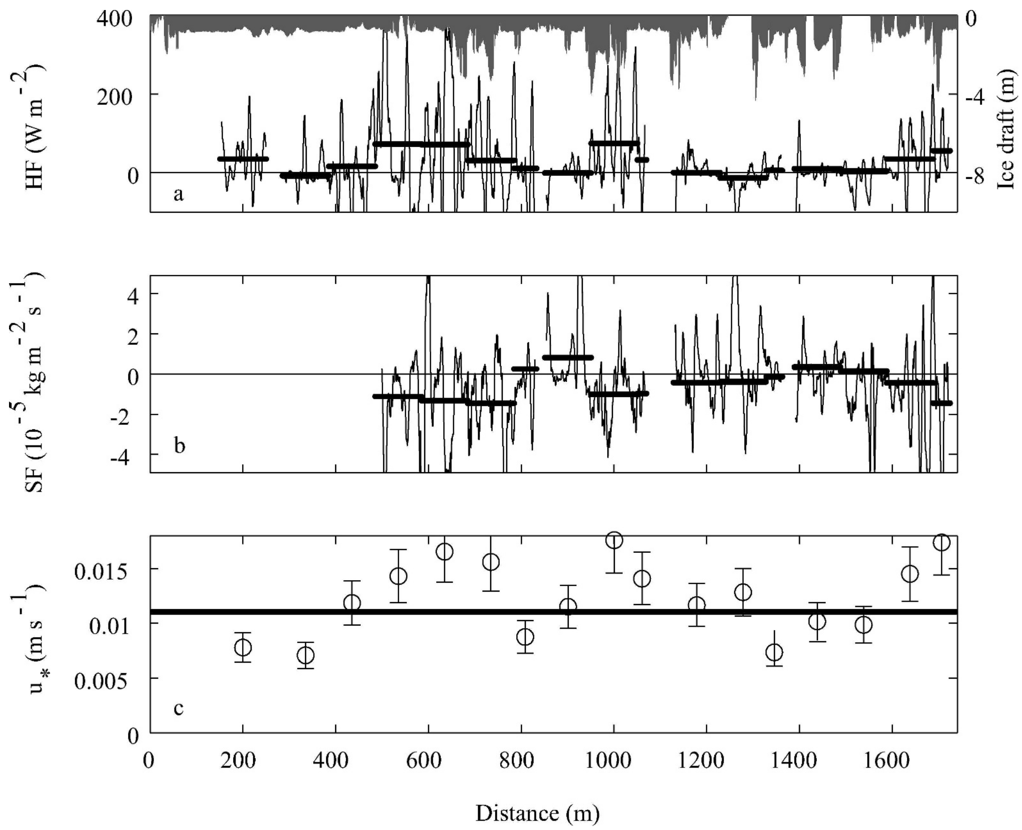

Fig. 7. AMTV run on day 213.0 (UT). (a) Heat flux with 100-m bin averages shown as horizontal lines (positive upward). (b) Salt flux (positive upward). (c) Friction speeds from the spectra of vertical water velocity and the 95% confidence interval and the bulk estimate of friction speed for this time from Fig. 3.

consistent with the attenuation of the heat flux with depth predicted by similarity theory for a horizontally homogenous steady boundary layer (McPhee 1983). We have only included in the run averages segments of heat flux that show a significant correlation, defined here as a correlation that differs from the peak correlation by at least 0.9 standard deviations using an empirical distribution based on random lags. While a 95% confidence interval is often used, this test had to be relaxed in order to make up for the relatively small segment size of 100 m. If no confidence testing is carried out, averages over a given run are clearly biased low. At the beginning of the experiment most runs were below 10 m, that is, below the mixed-layer depth (Fig. 4b). The AMTV runs before day 215 were under ice with leads of width 100 m or less (if any). After day 215, when most of the AMTV data were obtained under open water, heat fluxes in the mixed layer were downward because of radiative flux at the surface and the lack of ice to absorb heat by melting. The TIC heat flux from the downstream edge of the lead was always downward at both 3.5-m and 5.5-m depths as a result of radiative heating in the lead. On days 219–220, the downward AMTV heat flux at 5 m in the lead and the lead edge TIC heat flux were especially strong, similar to the downward shortwave radiation measured by the SHEBA Project Office, at 30–50% of the amplitude. The TIC in the hut near the ship (far from any leads) at no time indicated downward heat flux.

The AMTV and lead TIC both showed strong upward salt flux, well above the surface heat balance estimate, on days 219–220. The TIC near the ship also showed strong upward salt flux on day 219. The lead TIC on day 208 also showed strong upward salt fluxes.

Discussion

In this section the evolution of the upper ocean during summertime at SHEBA as described above is explained using scaling arguments supported by AMTV and environmental data. We show how the appearance of the surface fresh layer in leads can be predicted by a length scale which relates shear to buoyancy terms in the turbulent kinetic energy budget (the Obukhov length). The persistence of the layer is predicted by the internal Froude No., a measure of the hydrodynamic stability of a stratified shear flow. These two quantities lead in the direction of parameterizing the small-scale processes observed with the AMTV since they are based on the large-scale quantities of wind stress, bulk heat and salt fluxes, ice thickness distribution, and area coverage fraction.

Period I: surface traps meltwater—During June and early July surface melt drained laterally into low-lying areas of melt ponds and leads (Eicken et al. 2002). Higher ice permeability allowed more vertical percolation of melt in

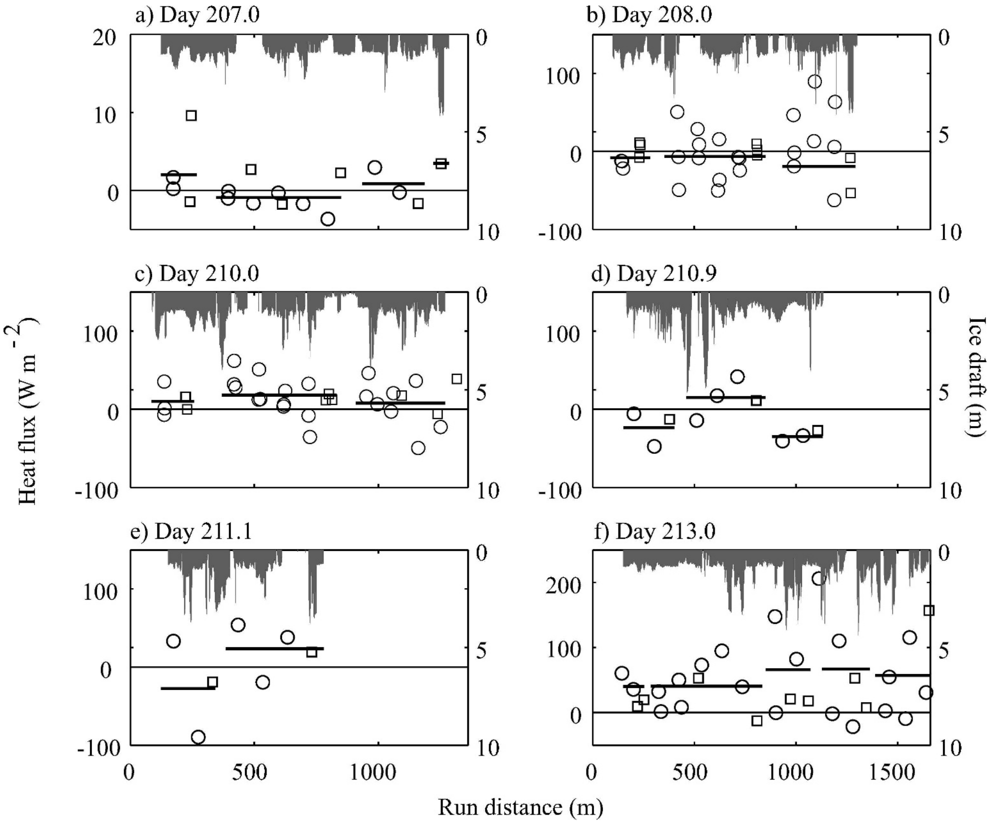

Fig. 8. AMTV heat flux and ice draft from (a) day 206, (b) day 208, (c) day 209, (d) day 210, (e) day 211, and (f) day 213 1998, at Sarah's Lake. AMTV depth was 10 m except for leg 2 for panel a (6 m) and all legs for panel f (8 m). On some days, more than one run following a similar track was achieved, and these runs were averaged to form the leg-average heat flux (solid horizontal lines). The 100-m segment averages for all runs are shown with circles. Heat-flux averages from portions of a leg less than one 100 m are shown with squares. Note the vertical scales are different for panels a and f.

mid-July, but lateral gradients in the pressure head caused fresh water to continue to build up in leads and cracks (Eicken et al. 2002; Paulson and Pegau 2001). Fresh water that entered the ocean at this time often formed an underwater ice layer or false bottom when it came into contact with the colder seawater: false bottoms tended to trap the runoff near the surface (Eicken et al. 2002). Underwater ice forms when fresh water and seawater at or near their respective salinity-determined freezing temperatures contact each other under quiescent conditions (Untersteiner and Badgley 1958; Martin and Kauffman 1974). Because solar heating was larger in leads, meltwater that collected there and the seawater beneath it were above their respective freezing temperatures, so underwater ice could not form. Strong and stable density gradients were often established near the lead surface, and low ice speeds (typically 5–7 cm s^{-1} in mid-July) allowed these fresh surface layers to persist for several weeks (*see* Fig. 2a).

The tendency for a buoyant layer to form in a lead can be described with an Obukhov length, L_0.

$$L_0 = \frac{u_{*0}^3}{\kappa \langle w'b' \rangle_0} \tag{5}$$

where $\kappa = 0.4$ and $\langle w'b' \rangle$ is the buoyancy flux: $g \rho^{-1} \langle w'\rho' \rangle$. At depths $1 < |L_0|$, turbulence is generated by shear, and buoyancy effects are small. An estimate of the Obukhov length beneath the lead can be made for days 190–207 (mid-Jul). The bulk estimate of surface friction speed rarely exceeded 0.005 m s^{-1} (Fig. 3a). An upper bound on the freshwater flux in the lead is found from the mean rate of surface ablation from day 190 to day 207: 1.5 cm day^{-1} (Perovich et al. 2003). Assuming all of the melt from ice without melt ponds drained into leads (about 75% and 5% of area, respectively, Perovich et al. [2002*b*]) implies a freshwater flux into the lead by Eq. 6 of about 7×10^{-5} kg m^{-2} s^{-1} or 5.3×10^{-7} W kg^{-1} for buoyancy flux.

$$\langle w'S' \rangle_0 = w_{perc}(S_{ml} - S_{ice}) = \frac{\rho_i}{\rho}\frac{dh_i}{dt}(S_{ml} - S_{ice}) \tag{6}$$

The resulting Obukhov length is 0.6 m, less than the ice draft, meaning turbulent stress was too weak to cause vertical mixing of the fresh meltwater. The remaining 20% of the surface was melt ponds which are assumed to be isolated from the ocean during this period. If one assumes that the fresh water melt from un-ponded ice entered the ocean uniformly over the surface (at a melt rate of 1.5 cm day^{-1}) the Obukhov length becomes 9 m. If this had been the case, the mixed layer would have freshened earlier in the

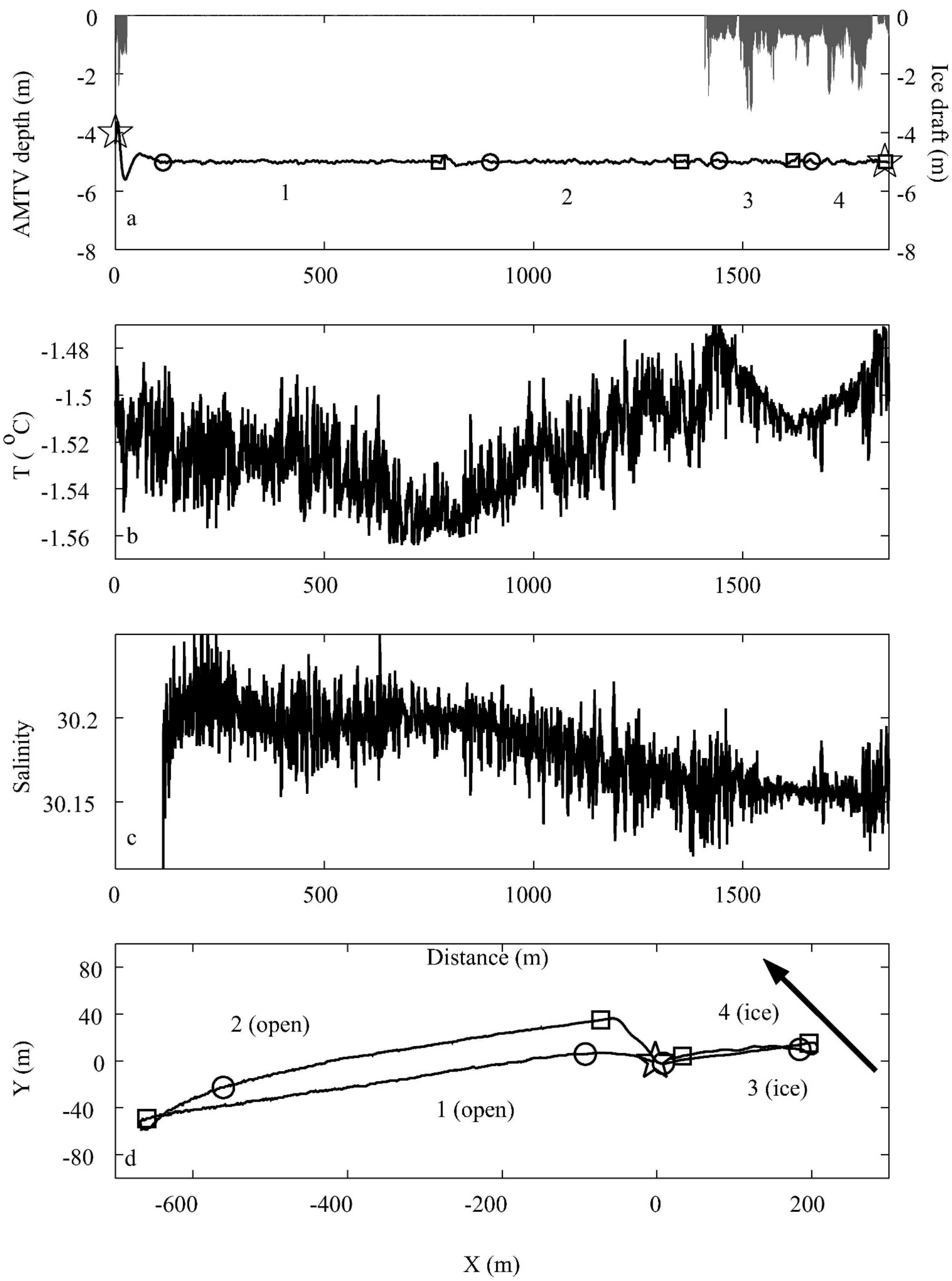

Fig. 9. AMTV run on day 219.9 (UT). Panel descriptions as in Fig. 6. Vehicle depth was 5 m, and ice draft averaged about 1 m with several ridges of about 3 m. After traveling for 800 m without leaving the lead (segment 1), the AMTV returned (segment 2) and continued to travel in the positive *x*-direction 200 m under the ice (segment 3) before returning to the origin (segment 4). The ice velocity vector of 15 cm s^{-1} is shown. The overall slope of salinity (particularly segment 1) is incorrect as a result of the nonlinear drift in conductivity.

summer. The Obukhov length determination for this period is consistent with the Large-Eddy Simulation (LES) model results of summer leads of Skyllingstad et al. (2005). Those authors show that above a critical wind stress, a fresh layer cannot form in the lead.

We can also examine the persistence of the fresh layer in the lead by approximating it as part of a two-layer system and calculating the internal Froude No. (*see* Fig. 2a):

$$Fr = \frac{U_{rel}}{\sqrt{g' H_l}} \tag{7}$$

where H_l is layer thickness and $g' = g(\rho - \rho_l)/\rho$.

We assume the layer moves with the ice, and the draft exceeds the layer depth. When the relative velocity of the layer (approximately the ice velocity) exceeds the wave speed at the interface, the ice can no longer block the flow of fresh water downstream, the layer begins to slide under

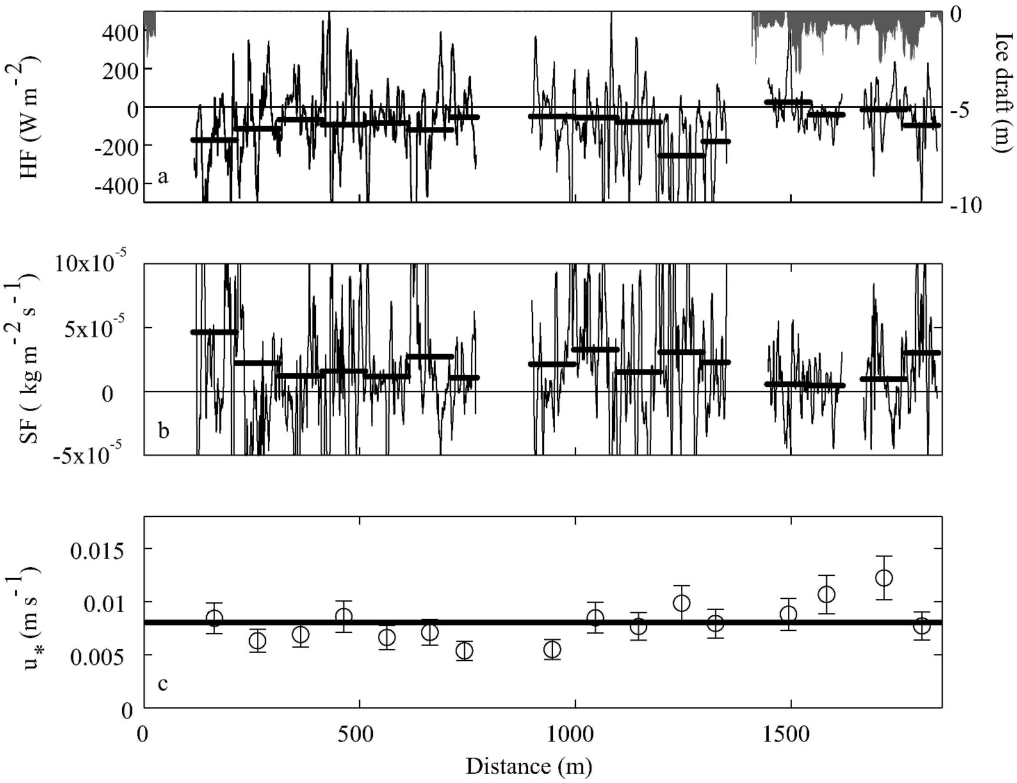

Fig. 10. Fluxes for AMTV run on day 219.9. Panel descriptions as in Fig. 7. The lead fluxes of heat and salt averaged 98 and 144 W m^{-2} and 1.7 and 2.4 × 10^{-5} kg m^{-2} s^{-1} (segments 1 and 2). The first 200 m of segment 1 were not included because it appears to have been contaminated (*see* Fig. 9).

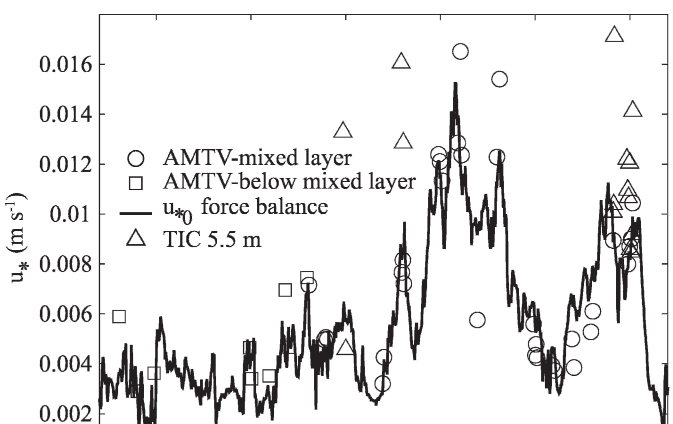

Fig. 11. Ice–ocean interface friction speed from steady-state balance of wind stress and Coriolis force as in Fig. 3 and AMTV run-averaged friction speed. On many days, especially before day 209 (28 Jul 98), the AMTV sampled multiple depths in the same run. Segments within a run that were above 10 m were averaged and closely follow the force balance estimate. These points are considered to be in the boundary layer. Averages of AMTV runs below 10 m are shown when no boundary layer data were available (before day 203.0). Lead-edge TIC observations at 5.5 m are also shown.

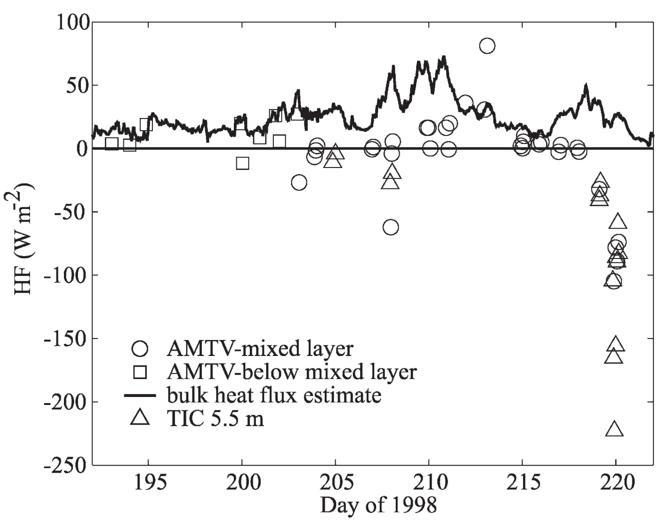

Fig. 12. Ice–ocean heat flux from bulk estimate as in Fig. 3 and heat flux from AMTV averages in the boundary layer. Averages of AMTV runs below 10 m are shown when no boundary layer data were available (before day 203.0). Lead-edge TIC heat fluxes are observed at 5.5 m. Only values of AMTV heat flux from 100-m segments that passed the significance test at a level of 0.9 standard deviations are included in the averages shown.

the ice (supercritical flow) and is ultimately entrained into the mixed layer possibly through a hydraulic jump (Skyllingstad et al. 2003). Prior to day 207, ice speeds were <10 cm s^{-1} and the layer salinity was <5, compared with 31 for the seawater. For a supercritical Froude No., the layer thickness would have to be <0.06 m. The lead layer could have increased beyond this thickness during a period of low ice velocity and, thus, survive the next significant ice movement. By day 185, the interface was at a depth of 20–30 cm (Paulson and Pegau 2001). On day 208, the ice velocity exceeded 10 cm s^{-1} for the first time in several weeks. By this time, the layer was 1.2 m thick, and $Fr = 0.3$ (ice speed of 0.12 m s^{-1}, layer thickness 1 m, and salinity jump of 26), suggesting the fresh water in the lead was still stable, and indeed a layer remained in the lead as the ice began to move (until day 212.5 according to the ROV data).

From day 206.5 to day 212.5, the fresh lead layer was gradually thinned by a combination of erosion from below, ice divergence, and hydrodynamic instability. The layer was shrinking at a rate of about 13 cm day^{-1} from day 206.5 to day 210.5 (based on ROV observations). While the ice velocity remained subcritical as the ice began to move on day 206.5, the layer was eroded away by turbulence generated upstream of the lead more quickly than meltwater was supplied. The lead-edge TIC observed large heat and salt fluxes consistent with warm, fresh water mixing downwards on day 208 (Fig. 12). After day 210, ice divergence may have also thinned the layer. On day 211, the thickness was 36 cm, and the ice speed was up to at least 0.20 m s^{-1}, so that $Fr = 0.8$. By the end of the day the layer was at 12 cm, and it was gone the next day (day 212.5). The order-one Froude No. on day 211 suggests the layer finally became thin enough to be hydrodynamically unstable and was rapidly flushed out of the lead (Fig. 2b).

The AMTV observations and Froude No. arguments are supported by the LES results of Skyllingstad et al. (2003). They showed a simulation for the period leading up to the onset of the wind event at SHEBA in which a fresh, 0.5-m layer under-plating the sea ice is ultimately blocked by a 0.54-m keel. No leads were present in this model, and relative ice–ocean velocity was brought up to 0.25 m s^{-1}. The AMTV observations in the period before day 210 (Fig. 8a,b) show small fluxes in the mixed layer under leads and ice, suggesting the melt water was indeed blocked in the lead, and this layer was restricting the generation of turbulent eddies at the vehicle run depths.

Period II: meltwater enters ocean—Two AMTV runs took place when the lead's fresh layer had just disappeared (212.9 and 213.1). Both runs showed downward salt flux and anomalously strong heat and momentum fluxes near ridge keels, while at the same time the bulk estimate of salt flux was in the opposite sense and the bulk heat and momentum fluxes in the same sense as the AMTV, but weaker. This could be the signature of a mechanism called overrunning overturns: the fresh warm plume from the lead may have been forced downward past adjacent ridges and under cooler, saltier (denser) water from the downstream side of the ridge (Fig. 2b). An unstable vertical-density gradient would result. Such overrunning overturns would enhance the turbulent mixing at the downstream lead edges. In general, this is a mechanism that may arise when a strong downward freshwater flux is upstream of little or no freshwater flux. Crawford et al. (1999) discuss evidence of this mechanism in the mixed layer under land-fast ice, but this is the first time evidence for such overturns has been observed in the vicinity of leads. Even if a horizontal density gradient did not play a role, it is possible that hydraulically controlled stratified flow resulted in a highly turbulent wake downstream of the keel, as suggested by the SHEBA ridge-keel modeling studies of Skyllingstad et al. (2003). In fact, the AMTV heat flux results from day 206 to day 213 are consistent with their large keel simulation (ridge keel extending 1 m below flat ice base, traveling at 43 cm s^{-1} over a strong stratification at about 0.5 m below the flat ice). Skyllingstad et al. (2003) report a hydraulic jump at around 10 m downstream of the ridge keel, and a turbulent wake that persists for about 50 m after 90 min of simulation (their fig. 14b). Heat fluxes under the keel and in the hydraulic jump and transition regions were much higher than upstream of the keel (their fig. 15b). Values ranged from 0 W m^{-2} to 30 W m^{-2} upstream to typical values of 50 W m^{-2} in the highly variable transition region, to >100 W m^{-2} at the keel itself. A similar situation exists in Fig. 8d and f, which show low heat fluxes under smooth ice and large heat fluxes under ridge keels. Skyllingstad et al. (2003) did not investigate the effects of a surface fresh-water flux.

During the windy period of day 210–214, when the mixed layer was freshening and experienced large stabilizing buoyancy flux at the surface, high levels of shear-generated turbulence deepened the mixed layer. The mixed layer deepening from 5 m to 16 m is consistent with the increased Obukhov length of about 24 m (using the spatial average salt flux of 4.6×10^{-5} kg m^{-2} s^{-1} and the maximum friction speed of 0.015 m s^{-1}). The average friction speed during this period of 0.01 m s^{-1} implies $L_0 =$ 7 m. In any case it was not possible for any fresh layer to form at the surface as in the earlier part of the summer, and what fresh layer did exist was removed.

Period III: quasi-steady boundary layer—The period after day 215 was characterized by weak freshwater fluxes and stronger winds. No freshwater layer was observed in the lead. A brief period of low wind stress (around day 215) may have allowed the surface melt to build up slightly in a layer in the lead (L_0 of 1 m), but not to a thickness to which it could be maintained, as indicated by a large Froude No. The ice velocity was >0.05 m s^{-1}, and any layer formed on day 215 would have to have been ≥ 2 cm thick for a Froude No. of order unity. As the ice velocity increased by day 220, a fresh layer would have to have been very thick to be maintained. From day 215 to day 220, the friction velocity increased to nearly 0.01 m s^{-1}, and the salt flux at the surface was about 2×10^{-5} kg m^{-2} s^{-1}. The Obukhov length increased to 16 m, the approximate mixed-layer depth. The data describe a steady internal boundary layer whose structure was determined from the time-dependent surface-boundary conditions of heat and salt fluxes, and stress (Fig. 2c).

Modeling studies

With the ideas of the internal Froude No. and the Obukhov length shown to be useful, if perhaps crude, in interpreting field observations, it is now our goal to examine the observations in a more quantitative way using numerical simulations. A simulation of the formation of a low-salinity layer and its flow over idealized ice topography will illustrate overrunning of dense water over less dense water downstream of a lead. The steady internal boundary layer of phase III is also simulated, and it is shown that horizontal profiles resemble closely those collected with the AMTV, strengthening the argument for the importance of including explicit ice topography and the mechanical forcing terms that result from it. For these purposes, the 3-D, non-hydrostatic model of Smith et al. (2002) has been modified for summertime ice–ocean boundary layer simulations. The along-lead dimension is chosen to be small in order to focus on the across-lead variability and its role in vertical mixing. These essentially two-dimensional simulations can allow for horizontal density gradients as well as mechanical forcing at lead edges, which was shown to trigger convective events in Smith and Morison (1998).

One of the modifications to the model for this study was the specification of the turbulent closure scheme. The momentum, temperature, and salt fluxes are expressed as covariances among the turbulent variables. These covariances are determined from mean (modeled) properties with first-order closure, so that the fluxes are modeled as property gradients multiplied by an eddy exchange coefficient, K. Stress is written in terms of local gradients.

$$\boldsymbol{\tau} = K\nabla\mathbf{u} \quad \text{or} \quad \langle u_i u_j \rangle = K\frac{\partial u_i}{\partial x_j} \tag{8}$$

where i and j each represent one coordinate direction. In our simulations, the diffusivity of heat and salt are equal to the eddy viscosity following an assumption of weak background stratification.

$$\langle w'T' \rangle = -K\frac{\partial T}{\partial z} \tag{9}$$

$$\langle w'S' \rangle = -K\frac{\partial S}{\partial z} \tag{10}$$

The first-order turbulent closure model (McPhee 1981, 1994) specifies the eddy viscosity as the product of characteristic turbulent velocity and local turbulent mixing length:

$$K = u_*\lambda \tag{11}$$

The local friction velocity, u_*, is the square root of the local kinematic stress, calculated from a previous estimate of eddy viscosity and the velocity shear profile.

$$u_* = \sqrt{|\boldsymbol{\tau}|} = \sqrt{K\left|\frac{\partial \mathbf{u}}{\partial z}\right|} \tag{12}$$

The friction velocity is set to a constant value in the surface layer (based on observations in this study). The surface layer is the region 2–4 m from the ice underside where the velocity profile is approximately logarithmic.

McPhee (1994) develops the mixing-length calculation for the stable or neutral mixed layer. In the surface layer, observations support the assumption of linear growth of the mixing length, λ, with distance to a maximum value (McPhee 1981, 1994). In the remainder of the mixed layer (the outer layer) the maximum value is calculated based on interfacial surface stress and planetary rotation and is bounded by stabilizing buoyancy flux through the stability parameter, η_*, which is ≤ 1.

$$\lambda = \min\left(\kappa|z|, \Lambda_* u_{*0}\eta_*^2 f^{-1}\right) \tag{13}$$

$$\eta_*^2 = \left(1 + \frac{\Lambda_* u_{*0}}{\kappa f R_c L_0}\right)^{-1} \tag{14}$$

where $\Lambda_* = 0.028$, an empirically derived constant, $R_c = 0.2$, the critical flux Richardson No. and, as above, $\kappa = 0.4$, and L_0 is the Obukhov length. The mixing length retains the constant value throughout the mixed layer, below which it is reduced in the strong stratification of the pycnocline. There the mixing length is calculated from Eqs. 13 and 14 using the *local* buoyancy flux and *local* stress. Horizontally averaged vertical profiles of friction velocity are multiplied by the mixing-length profile to form an eddy viscosity profile at every time step. The eddy viscosity does not vary in the horizontal. Both horizontal and vertical momentum flux terms use the same viscosity, although different background values are added (Table 1).

A pressure gradient term in the along-lead momentum equation ($-fU_i$) forces free-stream velocity (U_i) in the cross-lead direction. Doubly periodic flow is specified at the lateral boundaries, and no flow is allowed through the top and bottom boundaries. The bottom boundary is a free slip boundary for horizontal velocity, and no flux for either temperature or salinity. The top boundary is a flat surface lead surrounded by sinusoidal ice topography. There is a no-slip condition for horizontal velocity on the entire upper surface. Temperature and velocity are held constant in the domain representing ice. The salinity flux is zero at the ice–ocean interface—no ice melts or forms. In the lead a radiative heat flux is distributed with an extinction depth of 4 m. The lead salt flux is also specified, and it enters in the top grid cell only.

The 40-m wavelength of the ice topography is chosen from an estimate of the peak in the spectrum of ice draft gathered from the AMTV. The 2-m maximum thickness corresponds to a mean ice draft of about 1 m, and typical ridges with 2 m or 3 m of draft, as indicated by the AMTV data. The ice topography is greatly simplified by using only one sinusoidal component.

Numerical results—Two model experiments will be discussed: strong freshwater flux during boundary-layer spin-up (around day 207, *see* Fig. 2b) and freshening of a quasi-steady boundary layer (day 219.9, *see* Fig. 2c). The spin-up experiment applies a large freshwater flux in the

Table 1. Parameters for two three-dimensional numerical simulations. Spin-up refers to a period such as just before day 210 of the SHEBA experiment, 1998, when the fresh layer in the lead was shrinking. Quasi-steady refers to a period such as around day 219, 1998, when there was no freshwater layer in the SHEBA lead. Note that the y-dimension (along-lead dimension) is much smaller than the other dimensions, essentially eliminating y-derivatives.

Model parameters	Spin-up	Quasi-steady
Lead width (m)	80	480
Domain size (x, y, z m)	(240, 4.5, 10)	(1440, 9, 22.5)
U_i (m s^{-1})	0.07	0.15
Lead salt flux (10^{-5} kg m^{-2} s^{-1})	4.8	2.0
Lead heat flux (W m^{-2})	200	448
dx, dy (m)	0.5	1.0
dz (m)	0.1	0.25
dt (s)	0.5	0.5
Background A_z (m^2 s^{-1})	1×10^{-5}	1×10^{-6}
Background $A_{x,y}$ (m^2 s^{-1})	1×10^{-3}	1×10^{-5}
Initial velocity	$U=-U_i$ everywhere	steady 1−D BL solution

lead, a small ice velocity, and a uniform initial velocity profile relative to the motionless upper surface (Table 1). The salt flux in the model lead is set approximately to the flux estimated from the rate of decay of the fresh layer in the lead as observed early in the storm (day 206.5 to day 210.5). This does not represent the flux from the lead during the massive release 210.5 to 212.5 which is a factor of 2.5 larger. Initial temperature and salinity are uniform.

After one simulated hour, a layer of somewhat fresh water (change of 0.03) just over 1 m thick has formed in the lead (Fig. 13). As the layer is forced past the ice ridges, an unstable density gradient develops leeward of the ridge. The relatively fresh plume is forced downward as it is swept downstream, but dense, salty water remains in the ice depressions above. The freshwater plume has a maximum temperature in its core a few meters below the ice ridges, a signature of the lead surface near the downstream edge. There is strong shear in the top 5 m, particularly below the ridge keels. Over-running of dense water over light water is, therefore, simulated. However, overturning is not seen in the simulated velocity field, most likely because of the model diffusion. If the model could be run for a longer time, it is possible the salinity gradient could increase to a critical value at which point we could expect the model to show convective overturn in the lee of ridges. In addition, if the eddy viscosities could be reduced by a factor of two without numerical instability, overturns would be expected in the model.

This simulation suggests that horizontal variability in heat and salt flux, combined with ice topography, may enhance vertical mixing. The simulation in Fig. 13 may help us understand the AMTV fluxes during the large freshening event on days 210–215, which are not explained by 1-D models (Hayes et al. 2001; Hayes 2003). In the

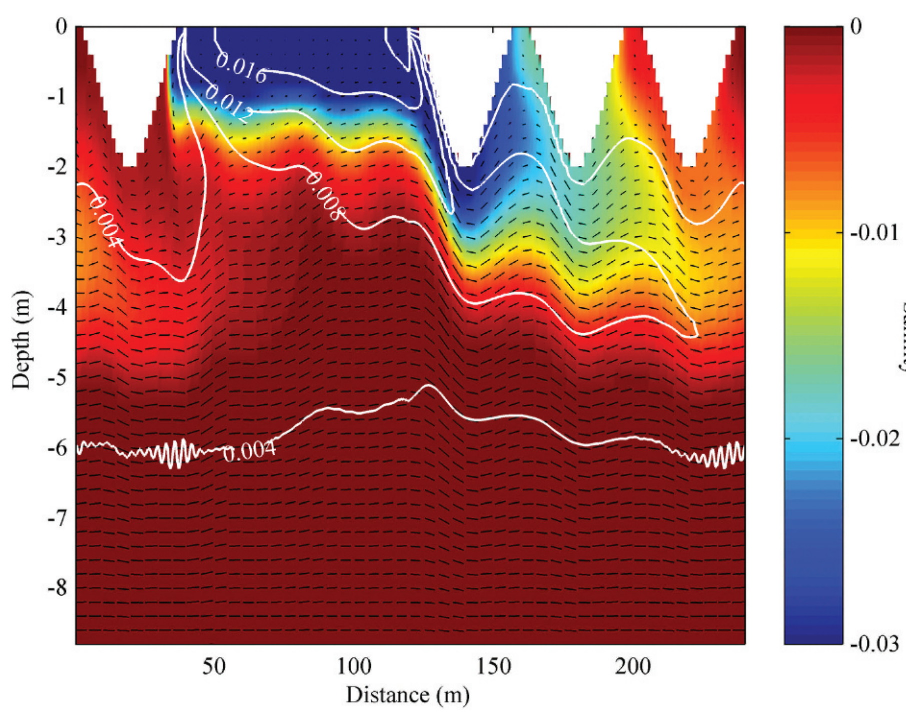

Fig. 13. Simulation of day 209 after 1 h with the non-hydrostatic, three-dimensional model in two-dimensional mode. Heat and salt fluxes at the lead surface are 200 W m^{-2} and 4.8 $\times$ 10^{-5} kg m^{-2} s^{-1}. *See* Table 1 for other simulation parameters. Salinity deviation is colored, temperature deviation is contoured. Velocity field is also shown; only one of every 10 vectors in the horizontal is shown. Flow is from left to right. Ice topography is at a fixed temperature and position, and there is zero salt flux at the ice–ocean interface.

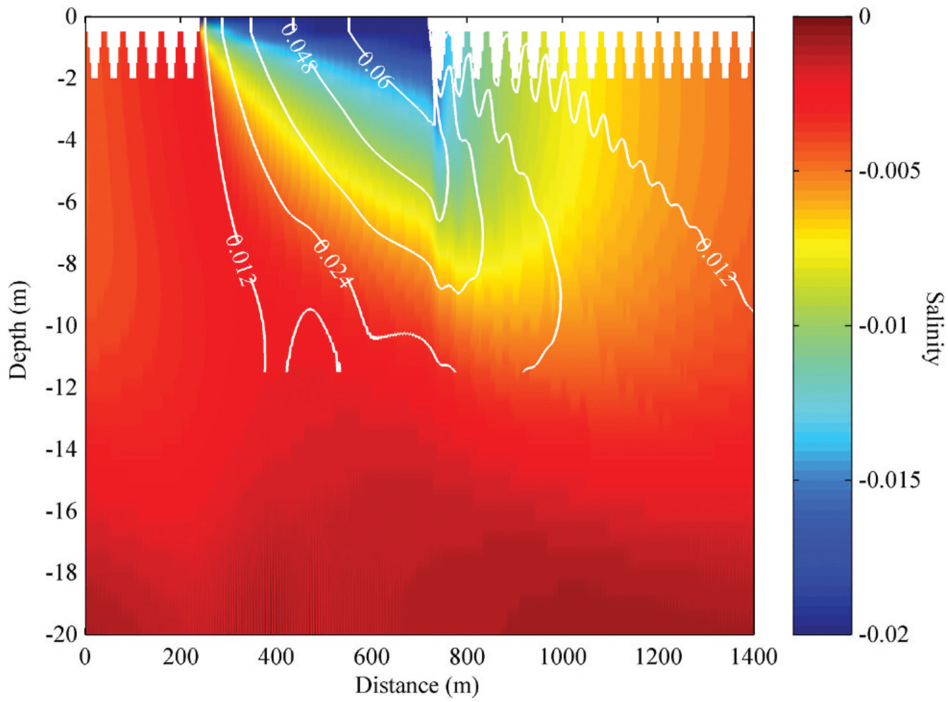

Fig. 14. Panel description as in Fig. 13, but for a simulation after 4 h using conditions approximating day 219.9. Ice topography is identical to that of Fig. 13. *See* Table 1 for run parameters. In these 4 h, the deep water traveled about 1500 m from left to right. Heat and salt fluxes at the lead surface are 448 W m^{-2} and 2 $\times$ 10^{-5} kg m^{-2} s^{-1}.

unstable region at depths of 3–4 m, the model predicts downward salt flux and upward heat flux. Unfortunately, there are no AMTV salt flux observations from the early part of this spin-up period. However, the AMTV observations on day 213 could be explained by the same overrunning mechanism: the location and signs of the fluxes at 5-m depth are consistent with these simulated fluxes.

Neither studies of Skyllingstad et al. (2003) nor Skyllingstad et al. (2005) predict downward salt fluxes. The former does not include lead freshwater flux boundary condition, since the top boundary consists of level ice and an isolated keel. The latter does not investigate the fate of the fresh-water layer after it escapes the lead. In fact, it does not allow for a mean relative ice–ocean velocity. Rather, the evolution of the fresh layer is driven by surface wind and density-gradient effects which can only be valid when the ice and lead surface layer move together during periods of blocking. More simulations in the vein of the one shown here need to be carried out to more fully characterize the tendency and possible effects of the unstable density gradient downstream of a region of stable surface buoyancy flux.

The second simulation is of the quasi-steady boundary layer on day 220 and agrees closely with observations, despite highly idealized ice-boundary conditions. Initial conditions for the experiment simulating day 220 are uniform temperature and salinity and a steady-state boundary-layer solution for the given free-stream velocity (assuming a flat upper surface). Other model parameters are listed in Table 1. Four hours into the simulation of day 219.9, fresh water entering in the top grid cell has been mixing downward, while at the same time carried downstream (Fig. 14). The salinity is lowest at the surface at the downstream edge of the lead. Temperature follows a similar pattern, with the warmest water at the surface at the downstream edge of the lead. The simulation is not strictly steady because as long as the lead fluxes are present, the boundary layer will become fresher and warmer, eventually building a shallow pycnocline.

Horizontal transects of model temperature, salinity, friction speed, heat, and salt flux (Fig. 15) compare well with AMTV observations from day 219.9 (Figs. 8, 9). The horizontal temperature gradient at 5-m depth in the lead is nearly identical to the AMTV measurement from day 220: a rise of 0.01 K for every 100 m. Temperature decreases on a slightly steeper gradient downstream of the lead edge in both the model and observations. Model salinity in the lead freshens with downstream distance, but we cannot compare it with the salinity trend from the AMTV, because a slow drift contaminated the record. Model friction speed at 5 m increases from lead to ice: 0.007 m s^{-1} to 0.009 m s^{-1}, consistent with the AMTV observations. Heat flux at 5 m reaches about 130 W m^{-2} downward in the last 200 m of the lead, comparable to the AMTV lead averages for that run (98 W m^{-2} and 144 W m^{-2} downward for segments 1 and 2). Model heat flux at 5 m becomes upwards (nearly 100 W m^{-2}) immediately downstream of the lead edge and decays to about half that value over the next 400 m. Two of four 100-m segments under the ice indicate the heat flux was downward: 40 W m^{-2} and 97 W m^{-2}. (The other two did not pass the

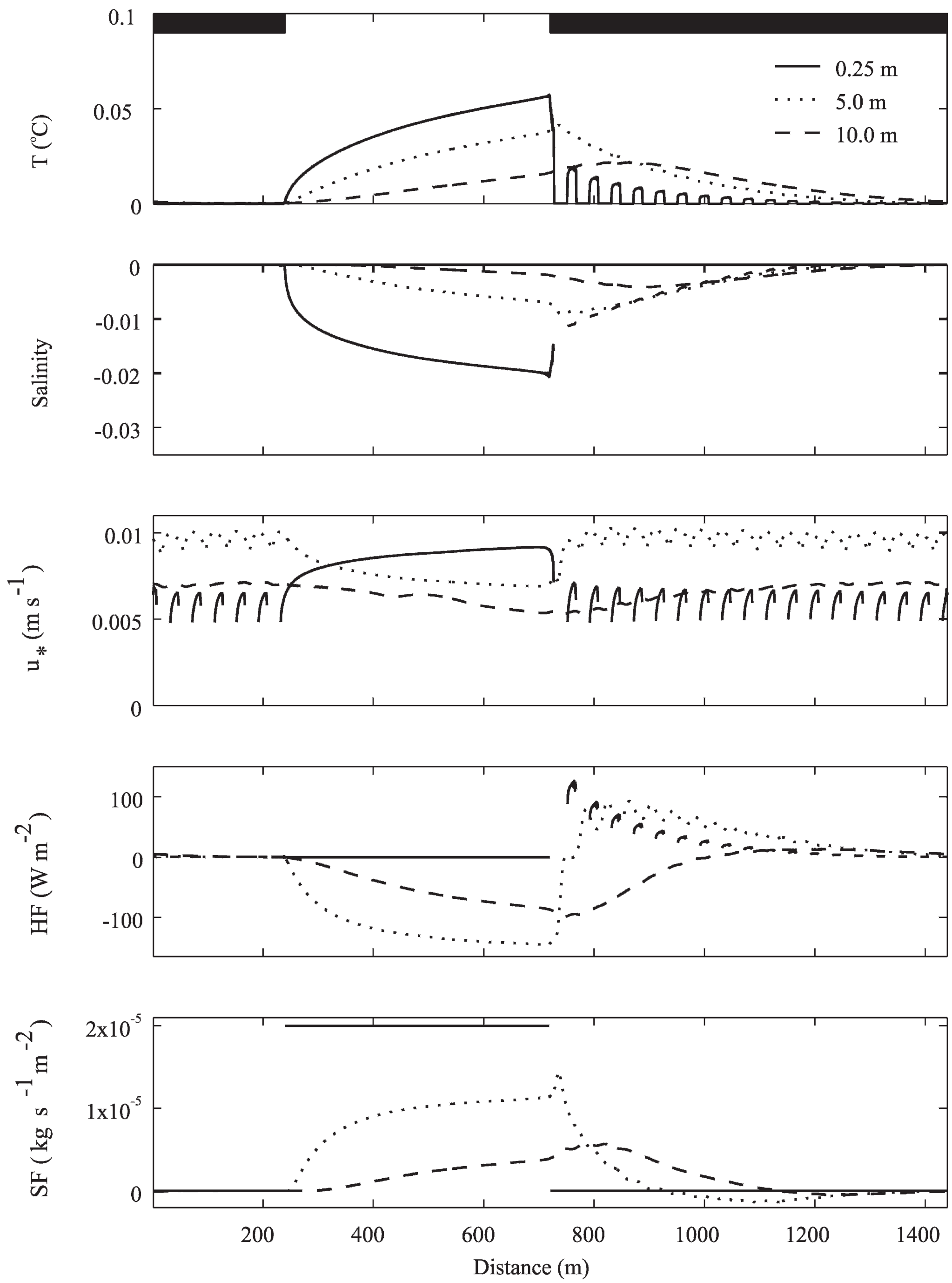

Fig. 15. Horizontal transects at surface, 5 m, and 10 m for same model run as Fig. 14. The lead is the 480-m-wide segment beginning at 240 m. Ice topography of Fig. 14 is present in regions indicated with a thick black line. The ocean is moving from left to right relative to the ice surface.

significance test.) Thus the AMTV under-ice heat-flux average is similar to a model transect between the depths of 5 m and 10 m. The model salt flux at 5-m depth in the lead approaches 1.2×10^{-5} kg m^{-2} s^{-1}upward, which is comparable to the AMTV lead values of 1.7×10^{-5} kg m^{-2} s^{-1} and 2.4×10^{-5} kg m^{-2} s^{-1}. The model salt flux decays by >50% in 100 m downstream. AMTV observations also suggest weaker salt fluxes under the ice, with those legs not passing the significance test.

The model ocean lost thermal energy at an average rate of 80 W m^{-2} to the ice during the run shown. The melt rate implied over the model domain is 2.6 cm day^{-1} (a salt flux of about 20% of that in the lead). Observations of ablation rate at the SHEBA bracket the model ice–ocean heat-flux results. On day 218 five ice-thickness gauges from 6 m to 51 m from the lead edge (adjacent to our hut and downstream of the lead) measured an average melt rate of 3.8 cm day^{-1}, while the SHEBA camp average was about 1.3 cm day^{-1} (Perovich et al. 1999). The model's inability to introduce the freshwater from the ice melt into the domain may have had an effect on the solution.

Topography and advective terms (not possible in a 1-D model) result in more rapid vertical mixing, as shown by the quick recovery of the boundary layer downstream of the lead. The mechanical forcing associated with an explicit lead edge also enhances mixing and recovery to the background boundary layer. Disagreements between the AMTV results and the model might be resolved by allowing ice melt in the model, or by refining the solar absorption or turbulent closure parameterizations. Taken on a whole, the numerical simulations indicate both the importance of explicit lead and ice morphology in reproducing observed horizontal profiles in the boundary layer, but also the tendency for unstable density gradients to form downstream of a region of stable surface buoyancy flux. These gradients may be responsible for the seemingly reverse (downward) salt fluxes near rough ice during the summertime at the SHEBA experiment.

Implications for larger scales

Surface fresh-water budget—The snow and ice melt at SHEBA did not enter the ocean immediately as it formed, nor did it uniformly cover the ocean surface. In addition to melt ponds, false bottoms, and the ice matrix itself, the meltwater remained in a fresh surface layer in leads (when the buoyancy flux was strong enough compared with the surface stress). The water that drained into leads built up in a strongly stratified layer because ice speeds were low. The release of fresh water from leads occurred in a relatively sudden, localized flush. The Obukhov length and Froude No. could be used to predict the formation and persistence of such a lead surface layer over large scales.

Large-scale models need to accurately simulate the vertical freshwater flux at the upper ocean surface in order to accurately simulate the ice-albedo feedback. Surface meltwater retention affects the ice-albedo feedback in at least two important ways: it lowers the albedo early in the summer through melt-pond formation, and it results in a strong freshwater flux that temporarily seals off thermal energy in the pycnocline from interacting with the ice base (Kadko 2000). As a first step in modeling the effect of meltwater retention on the mixed layer in a large-scale model, one could assume that all of the surface melt runs into leads (i.e., that ice is impermeable). This is a good assumption early in the melt season (until day 170 for SHEBA [Eicken et al. 2002]). In that case, the surface melt would be multiplied by the ratio of bare ice fraction to lead fraction to estimate the meltwater flux into leads. The Obukhov length could then be calculated from ice–ocean stress and the estimate of buoyancy flux at the lead surface. If the Obukhov length were larger than the ice draft, surface melt would enter the uppermost model grid cell immediately, otherwise, the surface melt could be held in a parameterized model surface reservoir until a critical Froude No. was reached, at which point the freshwater flux in the model would begin. As the melt season progresses, however, the lead flux is strongly dependent on the permeability of the ice and the surface melt rate which also must be considered in model parameterizations (Eicken et al. 2002). A promising step forward has been made by Holland (2003) who has modified a single-column ice–ocean coupled model to allow for fresh water to accumulate in the lead thickness class. Holland (2003) showed that the modification resulted in increased lateral melt rates, open-water formation, and amount of solar radiation, all of which strengthen ice-albedo feedback.

This simple model of meltwater delay would change the seasonal cycle of mixed-layer depth in large-scale models. Currently, Arctic Ocean models such as the model of Zhang et al. (1998) predict mixed-layer deepening throughout the fall, winter, and spring. In their model the freshwater gradually enters the mixed layer, the ocean is not capped off, and the mixed layer can provide heat to the bottom of the ice from early summer onwards. If, instead, the modeled mixed layer's jump to minimum depth is delayed until a flushing event, the sudden release of fresh water would place a tight lid on heat absorbed below the new shallow mixed layer until an autumn or winter storm deepened it.

It appears from the Arctic Ice Dynamics Joint Experiment (AIDJEX) (1975) and SHEBA (1997–1998) that the heat deeper in the mixed layer did not reach the surface until later in the autumn or winter, consistent with the meltwater retention scenario. We calculate roughly 5–10 MJ m^{-2} remain in the top 30 m from SHEBA observations, and Maykut and McPhee (1995) calculate 15–20 MJ m^{-2} for AIDJEX, mostly between 30 and 50 m. Storage in the upper pycnocline weakens the ice-albedo feedback, since solar energy stored in the upper ocean cannot reach the ice surface until later in the year when incoming solar radiation is weaker.

Surface heat budget—Horizontal variability in the summertime polar mixed layer at SHEBA was unexpectedly strong. Large upward heat fluxes and downward salt fluxes under ridge keels during a storm provide new evidence for a mechanism we call overrunning overturns. It resembles turbulent wakes in a stratified hydraulically controlled flow, or breaking internal waves at a strongly stratified interface but results from vertical shear in a horizontal density gradient. A 2-D model simulated observed horizontal mixed-layer structure and provided some additional evidence for the overrunning mechanism. A simple heat-balance calculation suggests a horizontally homogeneous ice–ocean heat flux is not always realistic (Hayes 2003). Horizontal inhomogeneity is problematic for large-scale models that use a single mixed-layer temperature for all ice thickness classes to calculate ice–ocean heat flux in a given grid cell. In reality, this temperature can vary significantly over a few hundred meters, as seen in AMTV observations from this study.

The most significant way in which small-scales influence the heat budget of the Arctic Ocean is probably lateral melting. Besides Sarah's Lake, eight leads within 30 km of SHEBA had a warm, fresh layer on day 203 (Richter-Menge et al. 2001). This layer caused extensive lateral melting at two leads instrumented by Perovich et al. (2003).

In fact, Perovich et al. (2003) partitioned the total energy expended on melting into lateral melting (5%), basal melting (18%), and surface melting (77%) on 20 July (day 201). In addition, heat stored in leads can be released to the mixed layer in a delayed fashion as a result of the highly stable fresh layers formed in early and mid-summer near the SHEBA site.

Changes in the observed heat content from day 210 to day 242 disagree with those suggested by a simple three-way balance between solar input, bulk-estimated ice–ocean heat flux, and upper ocean heat content (Hayes 2003). According to this balance, the ocean should have only cooled slightly around day 210, and then the heat content should have been increasing by 15 W m^{-2} more than observed from day 210 to day 242 (Hayes 2003). The problem lies with the bulk ice–ocean heat flux: it is less than the flux implied by bottom melting in Perovich et al. (2003), who show the energy used in bottom melting from 01 June to 31 August (day 152 to day 242) was roughly 155 MJ m^{-2}, compared with 130 MJ m^{-2} estimated from the empirical bulk heat-flux relation. After day 210, the ablation estimate of heat flux increases linearly while the bulk estimate increases sharply before leveling off.

The bulk estimate of ice–ocean heat flux could be low because after day 213 there was more floe edge, which experienced the higher temperatures of adjacent leads. The bulk heat flux formulation for bottom melt has been used successfully in the past (McPhee 1992; Maykut and McPhee 1995). It assumes a horizontally representative mixed layer temperature and friction speed. However, Perovich and Elder (2002) observed large melt rates after day 213 near lead edges, and floe perimeter was observed to increase four-fold at the same time (Perovich et al. 2002*b*). Horizontal variation in mixed-layer temperature over the scale of a single floe may be more important than previously (Maykut and McPhee 1995) thought. There is no doubt temperature at a single depth in the mixed layer can vary significantly over a few hundred meters (*see* Fig. 9).

The ice–ocean flux at ridge keels is also likely to exceed the bulk estimate. A significant increase in roughness (e.g., near ridge keels) may enhance the ice–ocean flux (Wettlaufer 1991), and in fact we observed such a case on day 213. Also, the largest summer melt observed at SHEBA was an old ridge (average of 25 W m^{-2}) (Perovich and Elder 2002). While the effect of ridge keels is greater at the greater ice speeds seen after day 210, the observed increase of melt near lead edges after day 210 was much larger than under keels (Perovich and Elder 2002).

Large-scale heat budget calculations need to accurately represent the ice–ocean heat flux, which varies on small scales. Horizontal variation in heat content and in ice–ocean stress both play a role. We assert the mean heat flux over the larger scales (multifloe) is dependent on lead fraction and floe perimeter. While reasonably effective, the bulk exchange formulation does not agree exactly with the observed average melt rates in late summer; these vary greatly depending on ice type and location. Ridges and lead edges thinned the most, especially after the lead fraction and ice–ocean stress increased (Perovich et al. 2003). Large-scale models must keep track of the floe perimeter and lead size, and adjust the ice–ocean heat flux for each ice thickness class accordingly. Further studies using AUVs could substantially increase our understanding of lead edge and ridge keel processes and their role in vertical exchange between sea ice and ocean.

The picture of spatial variability of the summer under-ice boundary layer that emerges from this study implies some improvements are possible in large-scale ice–ocean–atmosphere models. In particular, a delayed flux of surface meltwater and lead edge effects stand out as two issues that can and should be addressed, both with model parameterizations and future observational programs.

References

ANDREAS, E. L., C. W. FAIRALL, P. S. GUEST, AND P. O. G. PERSSON. 2001. The air–ice drag coefficient measured for a year over Arctic sea ice, p. 300–303. *In* Proceedings of the Sixth Conference on Polar Meteorology and Oceanography, 14–18 May 2001, San Diego. American Meteorological Society.

CRAWFORD, G., L. PADMAN, AND M. MCPHEE. 1999. Turbulent mixing in Barrow Strait. Continental Shelf Res. **19:** 205–245.

CURRY, J. A., J. L. SCHRAMM, AND E. E. EBERT. 1995. Sea ice–albedo climate feedback mechanism. J. Climate **8:** 240–247.

EBERT, E. E., AND J. A. CURRY. 1993. An intermediate one-dimensional thermodynamic sea ice model for investigating ice–atmosphere interactions. J. Geophys. Res. **98:** 10,085–10,109.

EICKEN, H., H. R. KROUSE, D. KADKO, AND D. K. PEROVICH. 2002. Tracer studies of pathways and rates of meltwater transport through Arctic summer sea ice. J. Geophys. Res. **107:** 8046, doi:10.1029/2000JC000583.

FLEURY, M., AND R. G. LUECK. 1994. Direct heat flux estimates using a towed vehicle. J. Phys. Oceanogr. **24:** 801–818.

HAYES, D. R. 2003. The heat and salt balances of the upper ocean beneath a spatially variable melting sea ice cover. Ph.D. thesis. Univ. of Washington.

———, AND J. H. MORISON. 2002. Determining turbulent vertical velocity and fluxes of heat and salt with an autonomous underwater vehicle. J. Atmos. Oceanic Technol. **19:** 759–779.

———, ———, AND M. G. MCPHEE. 2001. Summertime oceanic fluxes at SHEBA: Observations and steady 2-D modeling, p. 271–274. *In* Proceedings of the Sixth Conference on Polar Meteorology and Oceanography, 14–18 May 2001, San Diego. American Meteorological Society.

HOLLAND, M. M. 2003. An improved single-column model representation of ocean mixing associated with summertime leads: Results from a SHEBA case study. J. Geophys. Res. **108:** 3107, doi:10.1029/2002JC001557.

———, J. A. CURRY, AND J. L. SCHRAMM. 1997. Modeling the thermodynamics of a sea ice thickness distribution: 2. Sea ice/ocean interactions. J. Geophys. Res. **102:** 23,093–23,107.

KADKO, D. 2000. Modeling the evolution of the Arctic mixed layer during the fall 1997 Surface Heat Budget of the Arctic Ocean (SHEBA) Project using measurements of ^{7}Be. J. Geophys. Res. **105:** 3369–3378.

LEADEX GROUP. 1993. The LeadEx experiment, Eos. Trans. Amer. Geophys. Union **74:** 393396–397.

LUECK, R. G., AND F. WOLK. 1999. An efficient method for determining the significance of covariance estimates. J. Atmos. Oceanic Technol. **16:** 773–775.

MANABE, S., R. J. STOUFFER, M. J. SPELMAN, AND K. BRYAN. 1991. Transient response of a coupled ocean–atmosphere model to gradual changes of atmospheric CO_2, Part I: Annual mean response. J. Climate. **4:** 785–818.

Martin, S., and P. Kauffman. 1974. The evolution of under-ice melt ponds, or double diffusion at the freezing point. J. Fluid Mech. **64:** 507–527.

Maykut, G. A., and M. G. McPhee. 1995. Solar heating of the Arctic mixed layer. J. Geophys. Res. **100:** 24,691–24,703.

———, and D. K. Perovich. 1987. The role of shortwave radiation in the summer decay of a sea ice cover. J. Geophys. Res. **92:** 7032–7044.

McPhee, M. G. 1981. An analytic similarity theory for the planetary boundary layer stabilized by surface buoyancy. Boundary-Layer Meteorol. **21:** 325–339.

———. 1983. Turbulent heat and momentum transfer in the oceanic boundary layer under melting pack ice. J. Geophys. Res. **88:** 2827–2835.

———. 1986*a*. Analysis and prediction of short-term ice drift. Presented at Fifth International Offshore Mechanics and Arctic Engineering Symposium, 13–18 April, Tokyo. American Society of Mechanical Engineers.

———. 1986*b*. The upper ocean, p. 339–394. *In* N. Untersteiner [ed.], The geophysics of sea ice. Proceedings of the NATO Advanced Study Institute on Air–Sea–Ice Interaction. Plenum.

———. 1989. A rigid, cable-lowered instrument frame for measuring turbulence and internal waves in the Arctic. IEEE J. Oceanic Eng. **14:** 203–207.

———. 1990. Small-scale processes, p. 287–334. *In* W. O. Smith [ed.], Polar oceanography. Part A: Physical science. Academic Press.

———. 1992. Turbulent heat flux in the upper ocean under sea ice. J. Geophys. Res. **97:** 5365–5379.

———. 1994. On the turbulent mixing length in the oceanic boundary layer. J. Phys. Oceanogr. **24:** 2014–2031.

———. 2004. A spectral technique for estimating turbulent stress, scalar flux magnitude, and eddy viscosity in the ocean boundary layer under pack ice. J. Phys. Oceanogr. **34:** 2180–2188.

———, G. A. Maykut, and J. H. Morison. 1987. Dynamics and thermodynamics of the ice/upper ocean system in the marginal ice zone of the Greenland Sea. J. Geophys. Res. **92:** 7017–7031.

———, and J. D. Smith. 1976. Measurements of the turbulent boundary layer under pack ice. J. Geophys. Res. **6:** 696–711.

Morison, J. H., and M. G. McPhee. 1998. Lead convection measured with an autonomous underwater vehicle. J. Geophys. Res. **103:** 3257–3281.

———, ———, and G. A. Maykut. 1987. Boundary layer, upper ocean, and ice observations in the Greenland Sea marginal ice zone. J. Geophys. Res. **92:** 6987–7011.

Paulson, C. A., and W. S. Pegau. 2001. The summertime thermohaline evolution of an Arctic lead: Heat budget of the surface layer, p. 271–274. *In* Proceedings of the Sixth Conference on Polar Meteorology and Oceanography, 14–18 May 2001, San Diego. American Meteorological Society.

Percival, D. B., and A. T. Walden. 1993. Spectral analysis for physical applications: Multitaper and conventional univariate techniques. Cambridge Univ. Press.

Perovich, D. K., and B. Elder. 2002. Estimates of ocean heat flux at SHEBA Geophys. Res. Lett. **29:** 1344, doi:10.1029/2001GL014171.

———, T. C. Grenfell, B. Light, and P. V. Hobbs. 2002*a*. Seasonal evolution of the albedo of multiyear Arctic sea ice. J. Geophys. Res. **107:** 8044, doi:10.1029/2000JC000438.

———, and others. 1999. SHEBA: Snow and ice studies. Cold Regions Research and Engineering Laboratory, [CD-ROM].

———, T. C. Grenfell, J. A. Richter-Menge, B. Light, W. B. Tucker III, and H. Eicken. 2003. Thin and thinner: Sea ice mass balance measurements during SHEBA. J. Geophys. Res. **108:** 8050, doi:10.1029/2001JC001079.

———, W. B. Tucker III, and K. A. Ligett. 2002*b*. Aerial observations of the evolution of ice surface conditions during summer. J. Geophys. Res. **107:** 8048, doi:10.1029/2000JC000449.

Richter-Menge, J. A., D. K. Perovich, and W. S. Pegau. 2001. Summer ice dynamics during SHEBA and its effect on the ocean heat content. Ann. Glaciol. **33:** 201–206.

Skyllingstad, E. D., C. A. Paulson, and W. S. Pegau. 2005. Simulation of turbulent exchange processes in summertime leads. J. Geophys. Res. **110:** C05021, doi:10.1029/2004JC002502.

———, ———, ———, M. G. McPhee, and T. Stanton. 2003. Effects of keels on ice bottom turbulence exchange. J. Geophys. Res. **108:** 3372, doi:10.1029/2002JC001488.

Smith, D. C. IV, J. W. Lavelle, and H. J. S. Fernando. 2002. Arctic ocean mixed-layer eddy generation under leads in sea ice. J. Geophys. Res. **107:** 3103, doi:10.1029/2001JC000822.

———, and J. H. Morison. 1998. Nonhydrostatic haline convection under leads in sea ice. J. Geophys. Res. **103:** 3233–3247.

Stern, H. L., and R. E. Moritz. 2002. Sea ice kinematics and surface properties from RADARSAT synthetic aperture radar during the SHEBA drift. J. Geophys. Res. **107:** 8028, doi:10.1029/2000JC000472.

Untersteiner, N., and F. I. Badgley. 1958. Preliminary results of thermal budget studies on Arctic pack ice during summer and autumn, p. 85–92. *In* W. R. Thurston [ed.], Arctic sea ice, Publ. 598. National Academy of Sciences, National Research Council.

Uttal, T., and others. 2002. Surface heat budget of the Arctic Ocean. Bull. Amer. Meteor. Soc. **83:** 255–275.

Wettlaufer, J. S. 1991. Heat flux at the ice–ocean interface. J. Geophys. Res. **96:** 7215–7236.

Zhang, J., W. D. Hibler III, M. Steele, and D. A. Rothrock. 1998. Arctic ice–ocean modeling with and without climate restoring. J. Phys. Oceanogr. **28:** 191–217.

Received: 1 September 2007
Accepted: 18 April 2008
Amended: 23 May 2008